Nanoparticle heat-up synthesis: *In situ* X-ray diffraction and extension from classical to non-classical nucleation and growth theory

Vanessa Leffler[†§], *Sascha Ehlert*[†], *Beate Förster*[‡§], *Martin Dulle* [†], *Stephan Förster*[†§*]

[†]Jülich Centre for Neutron Science (JCNS-1/IBI-8), Forschungszentrum Jülich, 52425 Jülich, Germany
[§] Institute of Physical Chemistry, RWTH Aachen University, 52074 Aachen, Germany
[‡] Ernst Ruska Center, Forschungszentrum Jülich, 52425 Jülich, Germany

[*]Address correspondence to: s.foerster@fz-juelich.de

Abstract

Heat-up synthesis routes are very commonly used for the controlled large-scale production of semiconductor and magnetic nanoparticles with narrow size distribution and high crystallinity. To obtain fundamental insights into the nucleation and growth kinetics is particularly demanding, because these procedures involve heating to temperatures above 300°C. We designed a sample environment to perform *in situ* SAXS/WAXS-experiments to investigate the nucleation and growth kinetics of iron oxide nanoparticles during heat-up synthesis up to 320°C. The analysis of the growth curves for varying heating rates, Fe/ligand ratios and plateau temperatures shows that the kinetics proceeds *via* a characteristic sequence of three phases: an induction Phase I, a final growth Phase III, and an intermediate Phase II, which can be divided into an early phase with the evolution and subsequent dissolution of an amorphous transient state, and a late phase, where crystalline particle nucleation and aggregation occurs. We extended classical nucleation and growth theory to account for an amorphous transient state and particle aggregation during the nucleation and growth phases. We find that this non-classical theory is able to quantitatively describe all measured growth curves. The model provides fundamental insights into the underlying kinetic processes especially in the complex Phase II with the occurrence of a transient amorphous state, the nucleation of crystalline primary particles, particle growth and particle aggregation proceeding on overlapping time scales. The described *in situ* experiments together with the extension of the classical nucleation and growth model highlight the two most important features of non-classical nucleation and growth routes, *i.e.* the formation of intermediate or transient species, and particle aggregation processes. They thus allows to quantitatively understand, predict and control nanoparticle nucleation and growth kinetics for a wide range of nanoparticle systems and synthetic procedures.

Keywords

nanoparticles, X-ray scattering, nucleation, growth, kinetics

Nanoparticles are attracting wide interest due to their exceptional properties enabling a wide range of applications in the fields of optoelectronics, bio-labeling, catalysis, and reinforced materials. [1] Therefore, optimized synthetic procedures have been established to control nanoparticle size, shape, and crystallinity. Further advancement of methods for nanoparticle synthesis require a deeper understanding of the nucleation and growth process and its kinetics, which can be complex and can occur over a wide range of time scales. Classical nucleation and growth theory has in many cases been successfully applied to describe and predict particle growth kinetics and size distributions. However, there are many phenomena observed during nanoparticle nucleation and growth such as the existence of amorphous precursor particles, liquid precursor phases, oriented attachment and aggregative growth processes that cannot satisfactorily be accounted for within the classical framework. [2] This currently makes the understanding of the nanoparticle nucleation and growth processes and predictions of the final nanoparticle size and shape very difficult.

The elucidation of these complex nanoparticle nucleation and growth phenomena requires *in situ* techniques to determine nanoparticle size, crystallinity, and chemical composition over a large range of time scales reaching from early precursor reactions, metastable intermediate and aggregated states to the final growth states. In recent years, the development of powerful *in situ* scattering and spectroscopic methods has significantly helped for a better understanding of nucleation and growth phenomena. In particular, small- and wide-angle X-ray scattering (SAXS, WAXS) employing third generation synchrotron and lab-based X-ray sources have allowed to experimentally follow the precursor reactions and the subsequent nucleation and growth of nanoparticles over a large range of length and time scales. This methodology, often supplemented by *in situ* light and X-ray spectroscopy, has been applied to investigate the nucleation and growth of metal nanoparticles such as gold [3-14] and palladium [15,16] as well as II− VI semiconductors such as ZnO [17-20] and SnO [21].

For many important metal chalcogenide semiconducting and magnetic nanoparticles such as CdS, CdSe, PbS, PbSe, and Fe_3O_4 hot-injection or heat-up synthesis methods have been established providing the best means to reproducibly obtain narrow disperse crystalline nanoparticles in high yields. [22] Because of its simplicity, the heat-up method using metal oleate precursors is highly advantageous for scale-up, as demonstrated by the production of iron oxide nanoparticles in tens of grams from single batch reactions. To follow the reaction kinetics *in situ* requires to monitor nucleation and growth processes at temperatures much higher than 100°C, representing a considerable challenge for scattering and spectroscopic experiments. Abecassis *et al.* were the first to study the synthesis of CdSe nanoparticles in octadecene up to temperatures of 240°C using *in situ* SAXS/WAXS. [23,24] Lassenberger *et al.* investigated the heat-up synthesis of iron oxide nanoparticles from iron pentacarbonyl precursors in dioctylether up to temperatures of 290°C. [25] These experiments provided important insights into the precursor decomposition and nucleation and growth kinetics during heat-up synthesis routes. In particular, for the iron oxide synthesis intermediate prenucleation clusters were clearly observed, which indicates that also the commonly used heat-up methods evolve *via* non-classical nucleation and growth routes. This raises the question whether non-classical growth processes are more generally observed for heat-up methods, and how these more complex non-classical growth mechanisms can be accounted for in describing the nucleation and growth kinetics.

Here we perform systematic *in situ* SAXS/WAXS experiments to follow the complete nucleation and growth kinetics of iron oxide nanoparticles for the very commonly used iron oleate heat up synthesis. The experiments are performed up to the so far highest temperatures of 320°C, thereby covering all relevant temperature and times scales from the early precursor decomposition to the final growth phase. For the investigations we used a lab-based high-brilliance X-ray setup together with a specially designed capillary heat-up device to reach high temperatures and to prevent the release of micro gas bubbles that interfere with the X-ray beam.

We find that the systematic variation of the most relevant synthetic parameters such as heating rate, final temperature, and iron/oleate ratio provide important insights into the nucleation and growth kinetics. We find that the mechanism of the oleate-based synthesis is mechanistically similar to that of the $Fe(CO)_5$-route, involving metastable amorphous precursor particles, but also evolving *via* aggregative growth processes. We therefore extend classical nucleation and growth theory to non-classical nucleation and growth theory by including amorphous precursor formation and particle aggregation. This extension allows a quantitative description of the measured growth curves. Furthermore, it provides a mechanistic basis to explain and compare the characteristic empirical nucleation and growth phases observed in the present study and reported in recent literature.

Results/Discussion

Classical nucleation and growth theory

One aim of the study is to expand classical nucleation and growth (NG) theory to consider more complex nucleation and growth scenarios involving (i) the transient formation of pre-nucleation species, (ii) aggregation processes, as well as (iii) the variation of temperature such as during heat-up synthesis. Starting point is the classical formulation of NG theory in terms of a chemical reaction that generates a reactive precursor species. [22] The nucleation process starts when the precursor species concentration exceeds its saturation concentration. This triggers a burst nucleation leading to a rapid consumption of the precursor species, such that its concentration quickly decreases below the saturation concentration, thereby ceasing the nucleation process. The formed nuclei subsequently grow until the precursor species has been completely consumed. This mechanism is known as the LaMer mechanism [28] with its characteristic separation of nucleation and growth phases leading to the formation of narrow disperse particles [29,30] as desired for many applications.

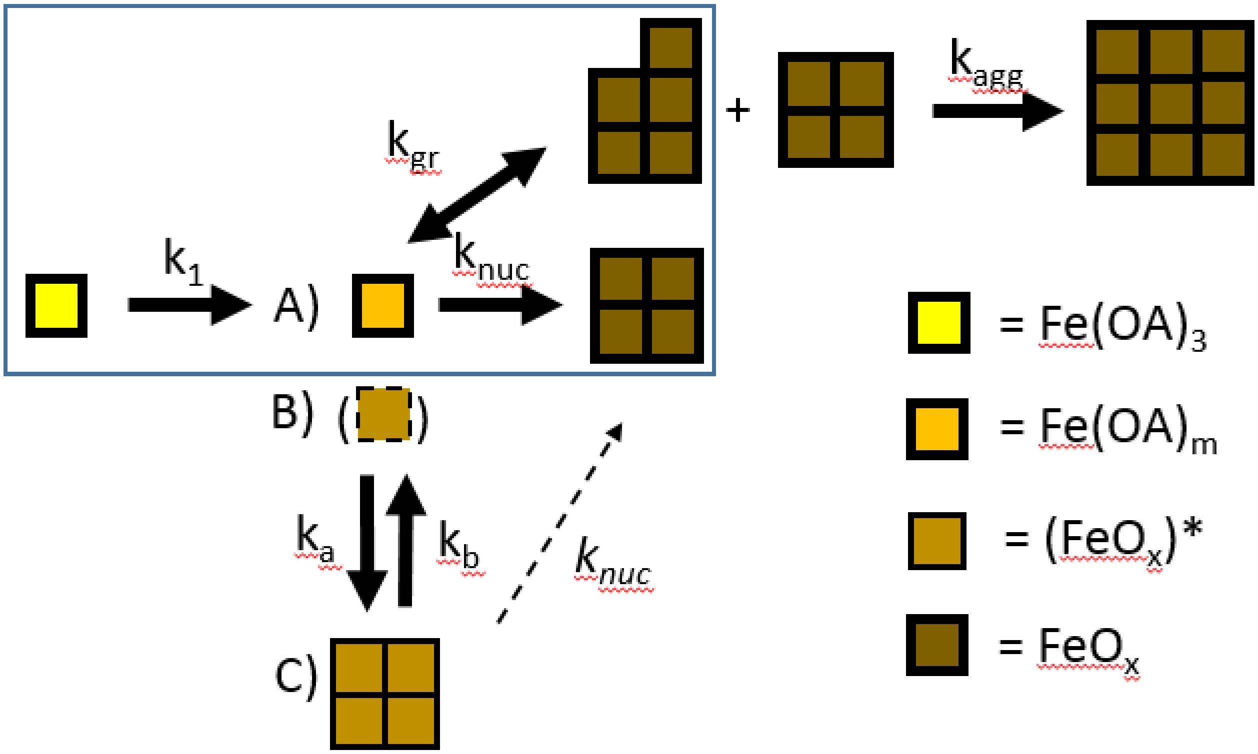

Fig. 1: Scheme of the nucleation and growth model. The framed classical model considers a precursor source $Fe(OA)_3$, which is decomposed into a reactive precursor species $Fe(OA)_m$, that is integrated as FeO_x-units into new nuclei or into growing nanoparticles. This model is extended by a reversible formation of amorphous units $(FeO_x)^*$ and the consideration of particle aggregation. This forms the basis

of the non-classical model comprising monomer-addition growth, aggregative growth, and growth *via* a pre-nucleation phase. The three possible paths *via* monomeric precursor species (A), oligomeric species (B), and pre-nucleation particles or domains (C) are indicated.

The classical NG model can be represented by a set of chemical reactions and their corresponding rate equations, which has been successfully used previously to quantitatively describe nanoparticle nucleation and growth. The full expression for classical NG theory has first been solved by Talapin *et al.* using Monte Carlo simulations to elucidate conditions for particle size focusing [31]. Refined numerical algorithms were derived by van Embden for comparison to the synthesis of CdSe nanoparticles [32] and by Mantzaris *et al.* [33] and Spalla *et al.* [4,6] to analyze the nucleation and growth kinetics of gold nanoparticles, providing valuable quantitative data for the growth rate constants. These algorithms assumed the presence of primary particles of a preset size distribution to calculate the subsequent nanoparticle growth. Chen *et al.* solved the complete set of reaction rate equations to explicitely take into account the nucleation of the primary particles during oversaturation. [13,20]

Considering the iron oxide nanoparticle synthesis in the present study, the generation of reactive precursor species occurs by a thermal decomposition reaction of Fe^{III}-oleate $Fe(OA)_3$

$$Fe(OA)_3 \overset{k_1}{\rightarrow} Fe(OA)_m \tag{1}$$

with a rate constant k_1. Eq. (1) is schematically written to indicate that $Fe(OA)_3$ loses OA-ligands and thereby is converted to the reactive precursor $Fe(OA)_m$ with $m < 3$. The actual chemical reaction is more complex, proceeding *via* the thermal decomposition of oleic acid (cis-9-octadecenoic acid) involving concurrent decarbonylation and decarboxylation reactions with the production of CO and CO_2. As a result oleic acid loses its carbonyl group such that the R-C=O···Fe ligand nanoparticle bond splits and the number of OA-ligands is reduced.

We investigated the oleic acid decomposition reaction by thermogravimetric analysis (TGA) as described in detail in the Supporting Information. We observe that initially ~1/3 of the OA-ligands is lost during a first thermal decomposition step in temperature range of 220 – 300°C. The remaining ~2/3 of the oleic acid decomposes in a second step in a temperature range 310 – 350°C. Since the first decomposition step occurs within the temperature range relevant for the nucleation phase during the heat-up synthesis, we take $Fe(OA)_m$ with $m \sim 2$ as the relevant reactive species in the kinetic reaction scheme as in Eq. (1).

For sufficiently high $Fe(OA)_m$ species supersaturation, nuclei will form consisting of FeO_x-units

$$Fe(OA)_m \xrightarrow{k_{nuc}} (FeO_x)_{nuc} \tag{2}$$

The reaction conditions used in the current experiments lead to the formation of magnetite Fe_3O_4, [26] which formally corresponds to FeO_x with $x = 4/3$. The use of $Fe(OA)_m$- and FeO_x-units throughout the chemical reaction and rate equations simplifies the stoichiometry. According to classical NG theory the nucleation rate constant k_{nuc} is given by

$$k_{nuc} = \beta \frac{V}{v_0} \exp\left[-\frac{\Delta G_c}{k_B T}\right] \tag{3}$$

with the rate $\beta = \frac{4k_B T}{9\eta v_0}$ given in terms of Boltzmann's constant k_B, the temperature T, and η the solvent viscosity. $v_0 = \frac{M}{\rho N_A}$ is the molar volume of the FeO_x-unit which is formed from the precursor $Fe(OA)_m$ and integrated into the particles. $v_0 = \frac{M}{\rho N_A} \sim 2.50 \cdot 10^{-29}$ m^3 is the molar volume of a FeO_x-unit, calculated from its molar mass $M(Fe_3O_4)/3 = 77.85$ g/mol, the Fe_3O_4 bulk density $\rho = 5.18$ g/cm^3, and Avogadro's constant N_A. V_{nuc} is the volume of the nucleated particle given by $V = \frac{4\pi R_{nuc}^3}{3}$ with the radius $R_{nuc} = \frac{R_{cap}}{\ln S}$ and the capillary radius $R_{cap} = \frac{2\gamma v_0}{k_B T}$. γ is the interfacial tension of the nanoparticle and $S = \frac{[Fe(OA)_m]}{[Fe(OA)_m]_{sat}}$ is the supersaturation, where $[Fe(OA)_m]_{sat}$ is the saturation concentration of the reactive $Fe(OA)_m$ –precursor.

The nucleation free enthalpy is given by

$$\Delta G_c = \frac{16\pi\gamma^3 v_0^2}{3(k_B T)^3 (lnS)^2} \tag{4}$$

During the nucleation phase new nuclei are formed continuously over a certain period of time. For numerical calculations subsequent distinct nucleation processes are considered, separated by time intervals Δt which can be arbitrarily small. Then cohorts of nuclei $J = 1,2, \ldots$ are formed at subsequent times $t_1, t_2, \ldots$ which grow by consumption of $Fe(OA)_m$

$$Fe(OA)_m \overset{k_{gr,J}}{\longleftrightarrow} \text{particle } J \text{ growth} \tag{5}$$

with the rate constant

$$k_{gr,J} = 4\pi R_J D N_A \frac{\left(1 - \frac{1}{S}\exp\left[\frac{R_{cap}}{R_J}\right]\right)}{\left(1 + \frac{D}{R_J k_{gr}}\right)} [P_J] \tag{6}$$

where D is the diffusion coefficient of the precursor Fe(OA)$_m$. It is calculated from the Stokes-Einstein relation $D = \frac{k_B T}{6\pi\eta R_0} \sim 2 \cdot 10^{-9}$ m^2/s, taking as the radius $R_0 = \left(\frac{3v_0}{4\pi}\right)^{1/3}$. R_J is the radius, and $[P_J]$ the concentration of the growing particles J. k_{gr} is the growth rate constant in units of m/s. The term $\left(1 - \frac{1}{S}\exp\left[\frac{R_{cap}}{R_J}\right]\right)$ describes the Ostwald ripening process. This term becomes negative for low values of the supersaturation S and small particle radii $R_J < R_{cap}$, leading to negative growth rates, *i.e.* the dissolution of the particles. This is formally indicated by the double arrow in Eq. (5).

For the experiments described in the present study we observe that during the growth phase the particle size distribution is sufficiently narrow such that the fraction of very small particles with $R_J \sim R_{cap}$ is negligibly small. Furthermore, the supersaturation S then has very small values, such that the Ostwald ripening term is ~1, meaning that Ostwald ripening has negligible influence on the final particle size distribution. We also observe that the growth is clearly surface-growth limited, as the ratio $\frac{D}{R_J k_{gr}} \sim \frac{10^{-9}}{10^{-9} 10^{-6}} \sim 10^6 \gg 1$. This is generally the case for nanoparticle growth as outlined in ref. [34]. We therefore made no further refinement to model the diffusion coefficient D by taking into account the possible association of the precursor Fe(OA)$_m$ with further stabilizing ligands.

Based on Equations (1) – (6) a set of coupled rate equations can be established for the consumption of the Fe(OA)$_3$-precursor, and for the formation and consumption of the reactive precursor species Fe(OA)$_m$ and FeO$_x$-units by the nucleation and growth reactions

$$\frac{d[Fe(OA)_3]}{dt} = -k_1[Fe(OA)_3] \tag{7a}$$

$$\frac{d[Fe(OA)_m]}{dt} = k_1[Fe(OA)_3] - k_{nuc}[Fe(OA)_m] \; - \textstyle\sum_J k_{gr,J}[Fe(OA)_m] \tag{7b}$$

$$\frac{d[FeO_x]_{nuc}}{dt} = k_{nuc}[Fe(OA)_m] \tag{7c}$$

$$\frac{d[FeO_x]}{dt} = \textstyle\sum_J \frac{[FeO_x]_J}{dt} = \sum_J k_{gr,J}[Fe(OA)_m] \tag{7d}$$

$$\frac{d[FeO_x]_{nuc}(t_J)}{dt} = [FeO_x]_J(t_J) \tag{7e}$$

Eq. (7e) indicates that the quantity $d[FeO_x]_{nuc}(t_J)$ of FeO$_x$-units nucleated at time t_J starts the cohort $\{P_J\}$ of J-particles. The set of coupled rate equations is written in terms of the time dependence of the molar Fe-concentrations of the precursor [Fe(OA)$_3$], the reactive species [Fe(OA)$_m$], the FeO$_x$-species incorporated into the nuclei [FeO$_x$]$_{nuc}$, and the Fe-species incorporated into the growing particles J,

$[FeO_x]_J$. For all nucleated and growing particles J, the molar Fe-concentrations $[FeO_x]_J$ can be converted to the particle concentration $[P_J]$ with knowledge of the particle radius R_J

$$[P]_J = \frac{v_0[FeO_x]}{V_J} \tag{8}$$

where $V_J = \frac{4\pi R_J^3}{3}$ is the volume of the particles. Here, we only consider nucleation *via* the monomer pathway as shown in Fig. 1. In principle, there could also be nucleation *via* the amorphous phase with a different nucleation rate constant, as the nucleation free energy will be different for both pathways. As there were no indications for this secondary nucleation, we did not supplement the kinetic scheme accordingly.

This set of rate equations can be numerically solved to quantitatively describe experimental growth curves in terms of classical NG-theory. [13] In the numerical solution each time step Δt allows for the nucleation of a new species J with a particle concentration $[P_J]$ calculated from the radius $R_{nuc} = \frac{R_{cap}}{\ln S}$, the corresponding volume $V_{nuc} = \frac{4\pi R_{nuc}^3}{3}$ and the amount of incorporated Fe-species $[FeO_x]_{nuc}$ (Eq. 7e). The algorithm is described in more detail in the Supporting Information. The calculations with Eq. (7) require the specification of the parameters given in Table I.

Table I: List of parameters used for the calculations of the growth curves using Eq. (7). Parameters are distinguished into parameters taken from literature, parameters where estimates from similar literature data could be made, and parameters consistently fitting all data sets, which were subsequently fixed to a particular value to minimize the number of free fit parameters. For the actual fits to the growth curves, only a single parameter, the growth rate constant $k_{gr,0}$ was varied.

Parameter	**Value**	**Comment**
Molar Mass M	$M(Fe_3O_4)$: 233.55 g/mol $M(FeO_{x=4/3}) = M(Fe_3O_4)/3$ = 77.85 g/mol	Lit.
Density ρ	5.18 g/cm^3	Lit.
Viscosity η	1 mPas	Lit.
Diffusion coefficient D	$2 \cdot 10^{-9}$ m^2/s	calculated
Temperature T	100 – 320 °C	varied during heat-up synthesis
Saturation concentration $[Fe(OA)_m]_{sat}$	$[Fe(OA)_m]_{sat,0} = 1 \cdot 10^{-7}$ mol/m^3 ΔE_{sol} = 20 kJ/mol $[Fe(OA)_m]_{sat} = 1.3 \cdot 10^{-9}$ mol/ m^3 @ 280°C	prefitted, then fixed prefitted, then fixed

Interfacial tension γ	γ = 450 mN/m	prefitted, then fixed
Reaction rate constant k_1	$k_{1,0}$ =3.0$\cdot$10^5 mol/m$^3\cdot$s ΔE_1 = 95 kJ/mol k_1 = 3.2$\cdot$10^{-5} mol/m$^3\cdot$s @ T = 280°C	prefitted, then fixed from TGA
Growth rate constant k_{gr}	$k_{gr,0}$ = 5.8 - 17$\cdot$10^4 m/s ΔE_{gr} = 110 kJ/mol k_{gr} = 2.4 – 7.0$\cdot$10^{-6} m/s @ T = 250°C	Fitted individually estimate from Lit.
Transient forward rate constant k_a	k_a = 0.01 mol/m$^3\cdot$s	prefitted, then fixed
Transient backward rate constant k_b	k_b = 0.02 mol/m$^3\cdot$s	prefitted, then fixed
Aggregation rate constant k_{agg}	$k_{agg,0}$ =1.0$\cdot$10^{12} mol/m$^3\cdot$s ΔE_{agg} = 110 kJ/mol k_{agg} = 4.1$\cdot$10^1 mol/m$^3\cdot$s @ T = 280°C	prefitted / fixed estimate from Lit.

Non-classical nucleation and growth theory

Classical NG theory is considering nucleation and growth from simple monomeric precursor species such as the reactive oleate species Fe(OA)$_m$, or neutral metallic Me^0-species such as Au^0 or Pd^0. Experiments frequently demonstrate the existence of non-classical nucleation and crystal growth processes that are distinct from the classical route. Examples are (i) the observation of amorphous nanoparticle precursors, which subsequently transform into crystalline particles, (ii) the formation of liquid phases that transform into crystalline particles through aggregation and dehydration, and (iii) particle aggregation and oriented attachment, which occurs by repeated attachment events of crystalline particles on specific crystal facets [2].

To extend classical NG-theory to include non-classical-NG pathways we consider two basic processes: (i) the transient reversible formation of a pre-nucleation species, and (ii) irreversible particle aggregation. The first process can describe e.g. the formation and transformation of amorphous precursors or liquid precursor phases, and the second process can be used to describe aggregation and oriented attachment. These two processes extend the classical monomeric growth model to aggregative growth, and are generic such that they can be specified and refined to more specific non-classical nucleation and growth processes.

Transient pre-nucleation species

The pre-nucleation species are often amorphous clusters or particles that are more rapidly formed than crystalline particles. For a non-crystalline phase the volume free energy ΔG_V is generally lower compared to the crystalline phase, which corresponds to a higher saturation concentration, thus making nucleation less likely. However, if also the surface free energy ΔG_A, which is proportional to the interfacial tension γ, is lower, nucleation can be faster compared to the crystalline state, as ΔG_{nuc} scales as γ^3 and only logarithmically depends the supersaturation S. (Eq. 4). Then the formation of amorphous particles can be kinetically favored. For high supersaturation S the thermodynamic state of the system evolves from the nucleation and growth to the spinodal demixing regime, where phase-separated high-concentration domains can be formed. Often demixing and phase separation is not macroscopic, but rather microscopic, leading to the formation of stable domains of nano- to micrometer dimensions.

For both the formation of amorphous particles, and the formation of spinodal domains we consider their formation to be reversible, such that they are formed and subsequently dissolved during particle nucleation and growth. Then they can be formulated as a classical chemical equilibrium [22], with the corresponding reaction

$$Fe(OA)_m \underset{k_b}{\overset{k_a}{\rightleftharpoons}} (FeO_x)^* \tag{9}$$

with the rate constants k_a for the forward, and k_b for the backward reaction.

Particle aggregation

Particle aggregation is a multistep process which can be described by a set of irreversible aggregation steps leading to an aggregation number n,

$$2\,A_1 \overset{k}{\rightarrow} A_{2,} \quad A_1 + A_2 \overset{k}{\rightarrow} A_{3,} \quad \dots \quad A_1 + A_{n-1} \overset{k}{\rightarrow} A_n \tag{10a}$$

$$A_i + A_j \overset{k}{\rightarrow} A_{i+j,} \quad i + j \leq n, \quad i,j \neq 1 \tag{10b}$$

Eq. (10a) describes monomer-cluster aggreation, and Eq. (10b) describes cluster-cluster aggregation. The maximum number n is determined by the number of A_1 primary particles. The classical treatment by Smoluchowski [35] considers diffusion-limited aggregation with particle size dependent rate constants

$$k_{ij} = \frac{2k_BT}{3\eta}\left(i^{1/3} + j^{1/3}\right)\left(i^{-1/3} + j^{-1/3}\right) \tag{11}$$

This approach has been applied to oriented particle attachment processes of ZnS [36] and PbS [37], with a broad overview provided by Penn *et al.* for a large range of particle systems [2,38]. For k_{ij} we can estimate typical values for the example $i = j = 1$: With a value for the solvent viscosity $\eta = 10^{-3}$ Pa·s and the temperature for high-temperature synthesis T = 473 K (200°C), we obtain $k_{11} = \frac{8k_BT}{3\eta} \sim 1.7 \cdot 10^{-7}$ m^3/s or $1.1 \cdot 10^{7}$ m^3/mol.s which can be compared to experimental results.

Often, particle surface stabilization leads to closed association processes with a small and finite *n*. As an example, oriented attachment decreases the particle surface area of high-energy facets to reach a stable state of *n*-mers with low surface energy. Often, the attachment of only a few particles is observed, such that *n* is small. [38] The limitation to a finite and small *n* significantly simplifies the numerical treatment of the aggregation process. This has been used for quantitative treatment of aggregation considering only monomer-cluster aggregation (Eq. 10a) [36,37] or just the formation of dimers A_2. [38]

Therefore, we limit the present consideration to just the first three steps of monomer-cluster aggregation with the formation A_4 as the final particle, which does not undergo further association. It would be straightforward to extend the aggregation number to *n* > 4. For the present investigation, however, the limitation to *n* = 4 turns out to be sufficient. The corresponding rate equations are the following sequence of monomer-cluster aggregation steps

$$\begin{gathered} 2\,P_J^{(1)} \xrightarrow{k_{agg}} P_J^{(2)} \\ P_J^{(1)} + P_J^{(2)} \xrightarrow{k_{agg}} P_J^{(3)} \\ P_J^{(1)} + P_J^{(3)} \xrightarrow{k_{agg}} P_J^{(4)} \end{gathered} \tag{12}$$

or in general terms for an $(i, i' \rightarrow k = i + i')$-aggregation

$$P_J^{(i)} + P_J^{(i\prime)} \xrightarrow{k_{agg}} P_J^{(k)} \tag{13}$$

leading to the corresponding rate equations

$$\begin{gathered} \frac{d\left[P_J^{(i)}\right]}{dt} = \frac{d\left[P_J^{(i\prime)}\right]}{dt} = -k_{agg}\left[P_J^{(i)}\right]\left[P_J^{(i\prime)}\right] \\ \frac{d\left[P_J^{(k)}\right]}{dt} = k_{agg}\left[P_J^{(i)}\right]\left[P_J^{(i\prime)}\right] \end{gathered} \tag{14}$$

where the $\{P_J^{(1)}\}$ is the cohort of primary particles that have been formed during the *J*-th nucleation step, which undergo stepwise aggregation to cohorts $\{P_J^{(2)}\}, \{P_J^{(3)}\}, \{P_J^{(4)}\}$ and at the same time can grow by precursor addition (Eq. 7d).

A serious complication when considering simultaneous particle aggregation and growth is the exponentially growing number of cohorts after a growth/aggregation sequence. Since unimers and *i*-mers have different sizes and therefore grow at different rates, subsequent aggregation from grown unimers leads to a new cohort of *i*-mers, that has a different size compared to the grown cohort of already existing *i*-mers. *n* growth/aggregation steps with aggregation numbers up to i_{max} will generate n^{imax} cohorts. A numerical calculation typically involves 10^4 time and thus growth/aggregation steps. Limiting aggregation to 4-mers as in the present study will generate 10^{16} cohorts, a number which is prohibitively large for computations. This has so far prevented the consideration of simultaneous growth and aggregation as a much needed extension of classical NG-theory.

In the present study an algorithm with an averaging step after each growth/aggregation-step is introduced to merge the new emerging cohort of *i*-mers with the old cohort of *i*-mers to keep the number of cohorts constant and keep numerical calculations tractable. Details and consequences of the cohort averaging step are outlined in the Supporting Information. If the prenucleation reaction Eq. (9) and the aggregation reactions Eq. (14) are considered, we then only need to specify the rate constants k_a, k_b, and k_{agg} for numerical calculations. The corresponding values are summarized in Table I.

Non-classical nucleation and growth model

If the non-classical rate terms from Eqs. (9) and (14) are implemented into the set of coupled rate equations (7) we obtain the non-classical NG-model

$$\frac{d[Fe(OA)_3]}{dt} = -k_1[Fe(OA)_3] \tag{15a}$$

$$\frac{d[Fe(OA)_m]}{dt} = k_1[Fe(OA)_3] - k_a[Fe(OA)_m] + k_b[(FeO_x)^*] - k_{nuc}[Fe(OA)_m] \tag{15b}$$

$$-\sum_{(i)}\sum_J k_{gr,J}^{(i)}[Fe(OA)_m]$$

$$\frac{d[(FeO_x)^*]}{dt} = k_a[Fe(OA)_m] - k_b[(FeO_x)^*] \tag{15c}$$

$$\frac{d[FeO_x]_{nuc}}{dt} = k_{nuc}[Fe(OA)_m] \tag{15d}$$

$$\frac{d[FeO_x]}{dt} = \sum_{(i)}\sum_J \frac{d[FeO_x]_J^{(i)}}{dt} = \sum_{(i)}\sum_J k_{gr,J}^{(i)}[Fe(OA)_m] \tag{15e}$$

$$\frac{d[FeO_x]_{nuc}(t)}{dt} = [FeO_x]_J^{(1)}(t), \quad t = t_J \tag{15f}$$

$$k_{gr,J}^{(i)} = 4\pi R_J^{(i)} D N_A \frac{\left(1-\frac{1}{S}\exp\left[\frac{R_{cap}}{R_J^{(i)}}\right]\right)}{\left(1+\frac{D}{R_J^{(i)}k_{gr}}\right)}\left[P_J^{(i)}\right] \tag{15e}$$

Eq. (15f) indicates that the quantity $d[FeO_x]_{nuc}(t_J)$ of FeO$_x$-units nucleated at time $t = t_J$ starts the cohort $\{P_J^{(1)}\}$ of *J*-unimer particles.

Temperature dependence

Finally, for the description of heat-up reactions, the temperature dependence of the kinetic parameters in Table I need to be considered. For the rate constants we use the corresponding Arrhenius equations

$$k_1 = k_{1,0}\exp\left[-\frac{\Delta E_1}{RT}\right] \tag{16a}$$

$$k_{gr} = k_{gr,0}\exp\left[-\frac{\Delta E_{gr}}{RT}\right] \tag{16b}$$

$$k_{agg} = k_{agg,0}\exp\left[-\frac{\Delta E_{agg}}{RT}\right] \tag{16c}$$

For the precursor decomposition reaction (1), we determined the activation energy ΔE_1 = 95 kJ/mol by thermogravimetric analysis (TGA), which is described in detail in the Supporting Information.

Furthermore, we need to consider the temperature dependence of the solubility $[Fe(OA)_m]_{sat}$, for which we use an Arrhenius equation as well

$$[Fe(OA)_2]_{sat} = [Fe(OA)_2]_{sat,0}\exp\left[-\frac{\Delta E_{sat}}{RT}\right] \tag{16d}$$

To keep the number of variable kinetic parameters as small as possible for a quantitative analysis, we either used literature values (M, ρ, η), determined parameters by a separate experiment (ΔE_1), or made reasonable estimates from literature data (D, ΔE_1, ΔE_{gr}). Further kinetic parameters (γ, k_a, k_b, $k_{agg,0}$, $k_{gr,0}$, $[Fe(OA)_m]_{sat,0}$, E_{sol}) were determined by searching for values that consistently prefitted best to all experimental data sets. These values were subsequently kept constant during final fitting to each of the individual growth curves. For these final fits only a single parameter, the growth rate $k_{gr,0}$, was varied. The fact that the parameter values in Table I give a consistent description of all measured growth curves over a temperature range of 100 – 320°C at varying heating rates (3.3 – 20 K/min), iron/oleate ratios (Fe/OA = 2:1; 1:1; 1:0), and plateau temperatures (280 – 320°C) shows that the non-classical NG model based on Eq. (15) provides a good, useful and robust description of the experimental data. The achievable precision of the fitted values is ~10% with the exception of the interfacial tension γ and the saturation concentration $[Fe(OA)_m]_{sat,0}$. Since the nucleation free energy ΔG_{nuc} depends on the ratio $\frac{\gamma^3}{(lnS)^2}$ (Eq. (3)), the two parameters are not independent from each other. Thus a decrease of the interfacial tension can, within a certain limit, be compensated by a larger value of the saturation concentration. This is possible within a range of 20% for γ, otherwise good agreement with the experimental data cannot be obtained anymore.

Solving this set of coupled differential equations yields the concentrations $[P_J^{(i)}](t)$ and radii $R_J^{(i)}(t)$ of all particles $\left\{P_J^{(i)}\right\}$ that have been formed during the nucleation process. From the concentrations the size distribution $h(R,t)$, the mean radius $\overline{R}(t)$, and the relative standard deviation $\sigma_R(t)$ can be calculated and can be compared to the experimental data. The size distributions all correspond to log-normal distributions. During the initial growth stages the relative standard deviations σ_R were in a range of 0.20 – 0.25, decreasing to values between 0.09 – 0.14 at the late growth stages for all calculations. The set of coupled differential equations is solved using a Runge-Kutta fourth-order algorithm, which fulfills two important criteria for the kinetic model: (i) the calculated concentrations are always non-negative, and (ii) it conserves mass at all times. Details of the calculations are given in ref. [13] and in the Supporting Information.

In situ SAXS/WAXS heating setup

In situ SAXS/WAXS heat-up experiments have so far been reported to follow CdSe nanoparticle nucleation and growth at 230°C in a capillary [23,24], and at 290°C in a reaction flask, where samples were continuously drawn and measured in a flow-through capillary. [25] We aimed for a capillary heat-up experiment to follow the reaction continuously *in situ* under precise temperature control up to a temperature of 320°C. The challenge for oleate decomposition experiments is to reach a sufficiently high temperature of 320°C, and to prevent micro gas bubbles due to CO/CO_2-release from interference with the X-ray beam.

Therefore, we developed a temperature-controlled capillary/heating block setup where the reacting solution is placed within an X-ray transparent thin glass capillary (Fig. 9). This design then enabled reproducible *in situ* SAXS/WAXS experiments over the whole reaction temperature of up to 320°C and reaction times over many hours. The setup is described in detail in the Experimental Section and the Supporting Information.

Small-angle X-ray scattering

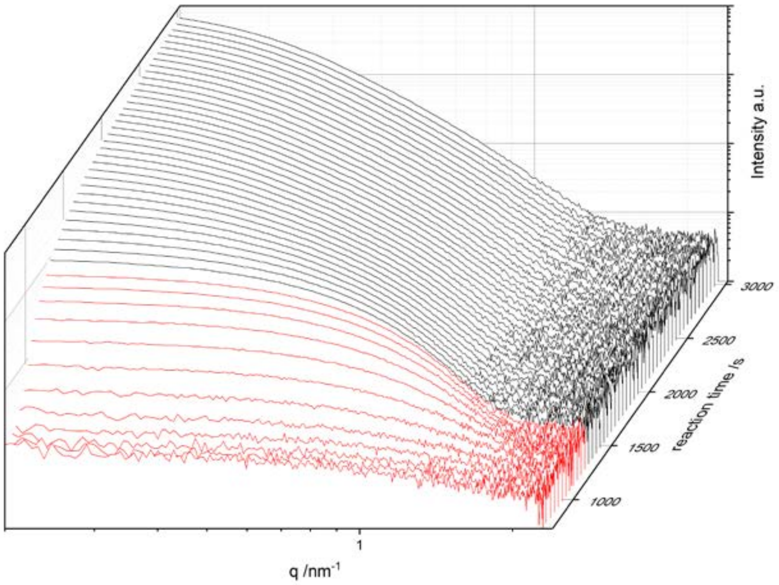

Fig. 2: Set of measured SAXS-curves during heat up (red) and constant final (black) temperature for a heating rate of 10K/min, a final temperature of 320°C, and an oleate/oleic acid 2:1 molar ratio. The evolution of the scattering intensity due to the formation of the nanoparticles during the heat up phase is well observable.

Small-angle X-ray scattering (SAXS) was used to follow the formation and growth of iron oxide nanoparticles during heating the precursor solution from 100°C to a target temperature of 280°, 300°, or 320°C at selected heating rates. We first investigated the nanoparticle growth kinetics for the reaction conditions with a target temperature of 320°C and a heating rate of 10 K/min. Fig. 2 shows the measured SAXS-curves for reaction times up to 3000 s. Each scattering curve was measured for 50 s. At the beginning of the experiment at times up to $t = 700$ s, corresponding to temperatures of 215°C, we observe very low, q-independent scattering intensities with a slight decay for $q > 1$ nm^{-1} indicating the presence of very small clusters. For times between $700 < t < 1300$ s, corresponding to temperatures of 215 – 320°C, we observe a pronounced increase of the scattering intensity at low *q*. The onset of the decay of the scattering intensity at the high-*q* end of the Guinier plateaus shifts to lower *q*, indicating the formation of nanoparticles with increasing size. For times t > 1300 s the increase of the scattering intensity and the shift of the Guinier regime eventually conclude, indicating the end of the nanoparticle growth. Thus, the full nucleation and growth period for the nanoparticle heat-up synthesis could be covered.

Growth Phases

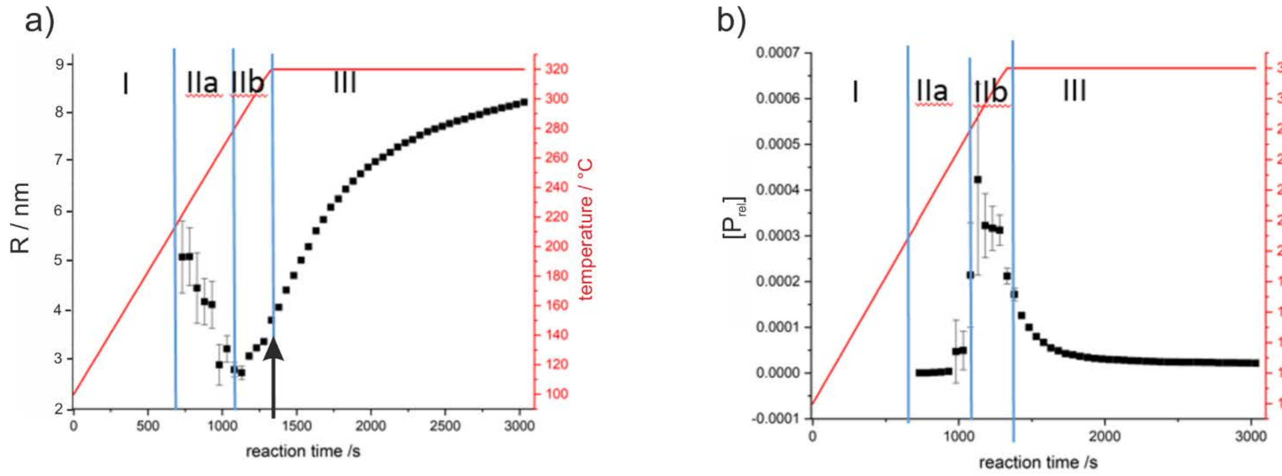

Fig. 3: Typical growth curve (a) and measured relative number of particles [P_{rel}] as a function of time. The four different characteristic phases I, IIa, IIb, and III are indicated. The red lines indicate the corresponding temperatures during the heat-up synthesis with a heating rate of 10K/min, a final temperature of 320°C, and an oleate/oleic acid 2:1 molar ratio. The arrow indicates a characteristic kink in the growth curve that is observed for heating rates of 3.3 and 10K/min. Error bars for [P_{rel}] at $t < 1000$ s, where [P_{rel}] is close to zero, are larger than the scale range and are not displayed.

The scattering curves are analyzed by fitting to the Guinier expression

$$I(q) = I(0)e^{-\frac{1}{3}q^2R_g^2}$$

where R_g is the radius of gyration, and $I(0)$ the scattering intensity at $q = 0$, from which the relative particle concentration $[P_{rel}] = I(0)/V$ is calculated. The Guinier analysis was chosen because it provides a well-defined measure of the z-average particle size R_g and weight-average particle number P_{rel} for an ensemble of particles having both size and shape polydispersity. As shown by the TEM-images in Fig. 8, many particles are not ideally spherical, but are rather faceted, which has similar effects on the scattering curves as size polydispersity, in particular leading to damping of formfactor oscillations. Details of the SAXS data analysis including a discussion of background subtraction during the *in situ* experiments are provided in the Supporting Information. For a comparison to the kinetic calculations the measured Guinier radii R_g were converted to an average particle radius $R = \sqrt{5/3}R_g$.

As an example, the growth curve R(t) and the relative particle concentration $[P_{rel}](t)$ corresponding to the data in Fig. 2 are provided in Fig. 3. In agreement with previous investigations of nanoparticle nucleation and growth kinetics, we can empirically distinguish characteristic phases. We first identify an induction phase (Phase I) which ends at t ~ 700 s, corresponding to a temperature of 215 °C, after which the first particles can be detected. Further, we can specify a final growth phase (Phase III) starting at a characteristic kink (indicated in Fig. 3a) in the growth curve at t ~ 1300 s, corresponding to the beginning of the plateau temperature of 320°C. In Phase III growth is dominated by precursor consumption until the final nanoparticle radius is reached. At intermediate times $700 < t < 1300$ there is an intermediate Phase II, where we can distinguish an early Phase IIa, where the measured radii R(t) decrease to a minimum at t ~ 1100s (Fig. 3a), corresponding to a temperature of 283°C, and where $[P_{rel}](t)$ is small and constant (Fig. 3b). This phase is followed by Phase IIb, where the radius is again increasing (Fig. 3a) and $[P_{rel}](t)$ goes through a maximum and subsequently decreases (Fig. 3b).

The characteristic time-dependence of R(t) and $[P_{rel}](t)$ already indicate that the heat-up synthesis route proceeds *via* non-classical states. The *decreasing* radii in Phase IIa are indicative for a dissociating transient state, and the decreasing $[P_{rel}](t)$-values in Phase IIb are a clear sign for particle aggregation. As discussed below, WAXS-data further support the existence of an amorphous intermediate state in Phase IIa. In Phase IIb crystalline nanoparticles are observed. The measured growth curves with the characteristic phases are well reproducible as shown by repeated experiments in the Supporting Information (Figs. S5, S6) Furthermore, the same characteristic phases can be identified in all subsequent experiments, where heating rates, end temperatures and oleic acid ratios have been systematically varied.

Heating rates (cNG vs ncNG)

The heating rate $\dot{T}$ is one of the three important reaction parameters determining the particle size distribution, which needs to be optimized for a particular nanoparticle synthesis. We investigated three different heating rates of $\dot{T}$ = 3.3, 10, and 20 K/min with the same start temperature T_a = 100°C and the same end temperature T_b = 320°C. A heating rate of 3.3 K/min is commonly selected for iron oxide nanoparticle synthesis.

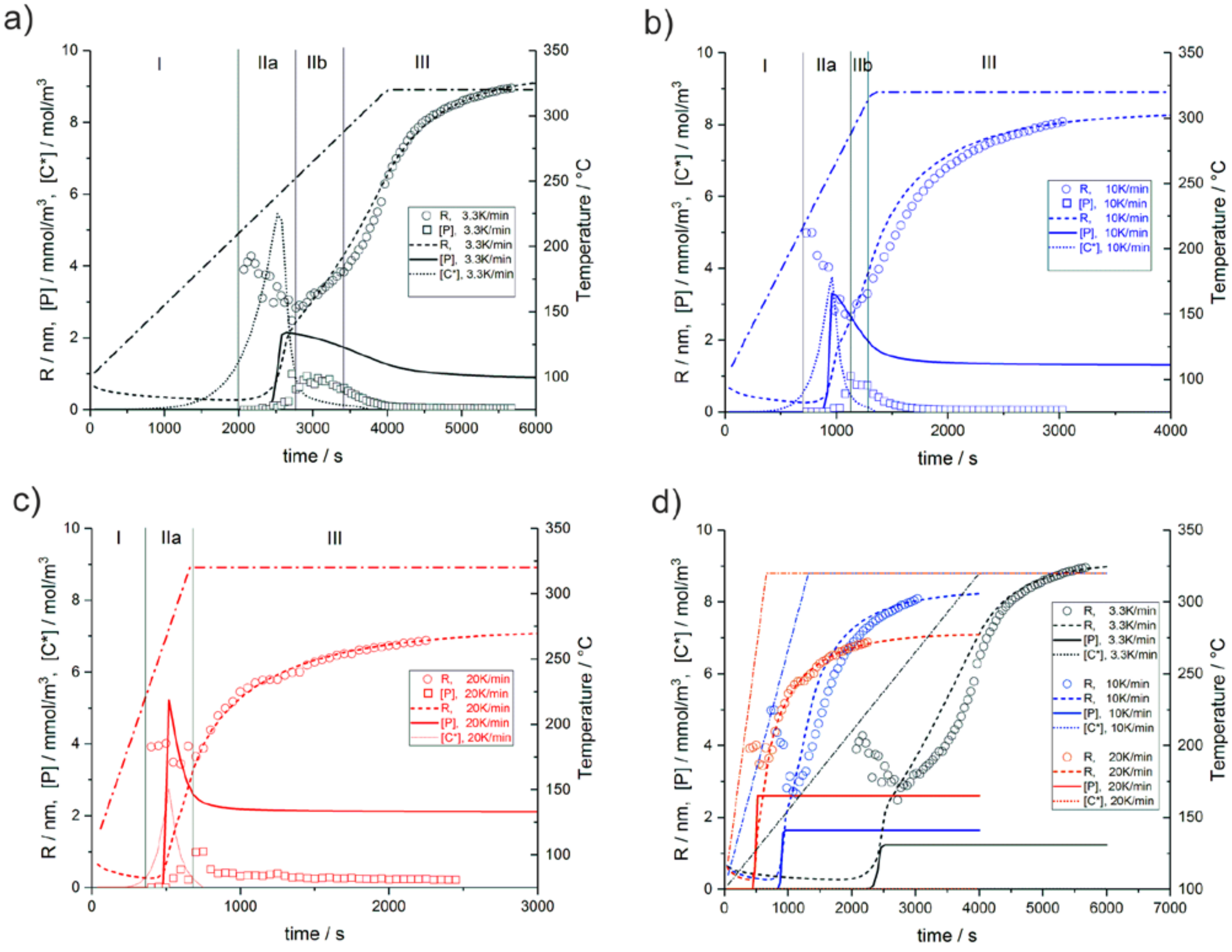

Fig. 4: Experimental growth curves R(t) (O) and relative particle concentrations [P_{rel}](t) (☐) for heating rates of 3.3 K/min (black; a, d), 10 K/min (blue; b, d), and 20 K/min (red; c, d) together with model calculations for the growth curves R(t) (dashed line), particle concentrations [P](t) (solid line), and transient phase concentrations [C*] = [FeO*] (dotted lines) for the non-classical NG-model (a, b, c) and

the classical NG-model (d). The dashed-dotted line indicates the temperature ramp (right y-axis). Characteristic kinetic Phases I, IIa, IIb, and III are indicated as described in the text. We observe that the non-classical NG-model nearly quantitatively describes the growth curves R(t) and provides a good description of the temporal evolution of the amorphous transient states and the aggregation processes for all heating rates (a-c). The classical NG-model quantitatively describes the measured growth curves only for fast heating rates, and cannot at all describe the observation of amorphous precursor and aggregated states (d).

Fig. 4 shows the experimental growth curves R(t) (O) and the relative particle concentrations $[P_{rel}](t)$ (☐) for the three heating rates $\dot{T}$ = 3.3, 10, and 20 K/min. The experimental data are displayed together with the calculated data (lines) for quantitative comparison. For all heating rates we observe the three characteristic phases I – III. For the growth rates $\dot{T}$ = 3.3, 10, and 20 K/min the induction Phase I ends at t^{I} = 2000s, 700 s, and 400 s. Phase IIa with the characteristic decrease of the measured radii extends to times t^{IIa} = 2800s, 1100s, and 600s. Phase IIb extending from the minimum of the radius until the kink in the growth curve is observed for t^{IIb} = 3400 and 1300s, with the fastest heating rate showing no kink in the R(t)-curve. The target temperature of 320°C is reached for times t_b = 4000s, 1320s, and 660s. The relative number of particles $[P_{rel}](t)$ always increases in Phase IIa, goes through a maximum in Phase IIb, and decreases to constant value early in Phase III. A comparison of Figs. 5a-c shows that higher heating rates lead to a correspondingly faster progression through Phases I, IIa, IIb, and III.

We first discuss the description of the growth curves R(t) in terms of a classical NG model as shown in Fig. 4d. We observe that the growth curves R(t) can be described reasonably well. The duration of the pre-nucleation Phase I, followed by a burst nucleation with a subsequent fast increase of the nanoparticle radius can be well reproduced, as well as the growth curve for the highest heating rate of 20 K/min. Just from analysis of the growth curve R(t) alone, a distinction between classical and non-classical NG models is often difficult. Further information on the evolution of the particle number concentration N(t) and the detection of transient states *via* specific properties such as crystallinity, density, and binding states, is necessary. This additional information is essential and can be provided by simultaneous *in situ* methods such as small- and wide-angle X-ray scattering (SAXS, WAXS) combined with light and X-ray spectroscopic methods (UV-Vis, EXAFS). [3-21,23-25] This has already been clearly demonstrated for a recent in-situ kinetic study on iron oxide nanoparticle nucleation and growth. [25] In model calculation with comparison to the experimental data from ref. [25] provided in the Supporting Information, we demonstrate that all three scenarios, *i.e.* classical NG-theory, extension to particle aggregation, and further extension to consider transient states can describe the growth curve R(t) nearly equally well.

However, for smaller heating rates classical NG overestimates the initial growth rates. Classical NG theory does not at all describe the decreasing particle concentration in Phase IIb and early Phase III because no aggregation steps are considered. Furthermore, it does not describe at all the observed decrease in particle size in Phase IIa, which is due to the existence of a transient amorphous phase.

Fig. 4 also shows the calculated growth curves R(t) using the non-classical NG-model (Eq. (15)), together with the calculated particle concentration [P](t) and the concentration of the transient state [C*](t) =[FeO*](t). The kinetic parameters used in the calculations are summarized in Table I. These parameters are kept constant for all experimental growth curves except for $k_{gr,0}$, whose value is fitted and varies slightly between 8.3 – $9.6 \cdot 10^4$ m/s as summarized in Table II.

With the non-classical NG model the growth curves R(t) can be well described not only for the highest heating rate of 20 K/min (Fig. 4c), but also for both lower heating rates of 10 and 3.3 K/min (Figs. 4a,b). Transient phase formation and nanoparticle aggregation can also be well described. In Fig. 4a the dotted curve shows the calculated concentration of the transient phase [C*] = [FeO*], which evolves through a pronounced maximum precisely in Phase IIa. This is the case for all heating rates as seen in Fig. 4a-c. Particle aggregation becomes evident from the decrease of the relative particle concentration $[P_{rel}](t)$. In Fig. 4 the solid curve shows the calculated particle concentration, which evolves through a maximum at the end of Phase IIa, and decays during Phase IIb and the early Phase III to reach a constant value. This is also the case for all heating rates. High rates of particle aggregation lead to the kink in the growth curve which separates Phase IIb from Phase III, as can be observed in Fig. 4a. The aggregation process is faster for $\dot{T}$ = 10 K/min, and thus Phase IIb is shorter (Fig. 4b). For the highest heating rate of 20K/min the aggregation process is finished so fast, that it does not lead to noticeable features in the growth curve (Fig. 5c). The calculated decrease of the particle concentration (solid line in Fig. 4a) due to aggregation reproduces the experimentally determined relative particle concentration $[P_{rel}](t)$ well. A slightly better agreement is expected if higher aggregation states >4 are considered, leading to a lower plateau value in Phase III.

The calculations also reproduce the observation that higher heating rates lead to faster aggregation, extending over 1000 s for $\dot{T}$ = 3.3 K/min (Fig. 4a), 400 s for $\dot{T}$ = 10 K/min (Fig. 4b) and only 100s for $\dot{T}$ = 20 K/min (Fig. 4c). Furthermore, the calculations also reproduce the observation that lower heating rates lead to larger particle radii. This is due to the lower number of nuclei formed, which upon consumption of the precursor grow to larger particles. The lower number of nuclei is related to the fact that nucleation for lower heating rates occurs already at lower temperatures, where according to Eq. (2) the nucleation rates are smaller. For consistency of the calculations we can consider the final particle concentration [P] = 1.24 mmol/m^3 (see Fig. 4a) with a radius R=8.95 nm. With v_0 from the FeO_x-species, we can calculate the molar concentration [FeO_x] from Eq. (9), which is 0.15 mol/l, close to nearly full conversion of 0.16 mol/, the initial $Fe(OA)_3$-concentration.

Thus, the extension to the non-classical NG-model is necessary and well reproduces all main features of the R(t)- and [P_{rel}](t)-curves for the three heating rates. It is noteworthy that the activation energy for the precursor formation k_1, as determined independently by thermogravimetric analysis, gives an accurate description of the temperature and heating-rate dependence for all nanoparticle nucleation and growth curves. The calculations allow to identify and quantify the kinetics of both the transient state and the particle aggregation process. It further shows that characteristic phases can be identified, even if the underlying kinetic processes are temporarily overlapping. In addition, it provides insights how heating rates control particle sizes, which is relevant for controlled nanoparticle synthesis.

A third conclusion is that a strict temporal separation of subsequent kinetic processes is not always possible, because individual reaction and aggregation processes such as the formation and dissociation of the transient state, particle nucleation, and particle aggregation are largely overlapping. As seen in Fig. 4, the transient state still exists during particle nucleation and particle aggregation. Particle aggregation starts already during the particle nucleation phase and extends all the way into the growth phase. During the early stages of particle formation all processes including transient state formation/dissociation, particle nucleation, particle aggregation and growth occur simultaneously. As observed from Fig. 5, some characteristic phases such as the induction phase (Phase 1) ending at t ~ 100 s, where no particles are yet present, and the late growth phase (Phase III) starting at t ~ 1000 s, where the particles grow predominantly by precursor consumption until they reach their final size, are still straightforward to be distinguished. Clearly, for a distinction of individual phases in the intermediate phase (Phase II) for 100 s < t < 1000 s more experimental information is needed, but in principle their distinction is justified.

Oleic acid ratio

We further analyzed the effect of the variation of the iron oleate/oleic acid ratio (Fe/OA). This ratio is usually varied to optimize nanoparticle synthesis conditions. We compared the frequently used Fe/OA-ratio of 2:1 to ratios of 1:1 and 1:0 for the same heating rate of 10 K/min and a plateau temperature of 320°C as shown in Fig. 5. We observe from the experimental growth curves R(t) that the Fe/OA-ratio does not affect Phases I and II, but has a pronounced effect in the growth Phase III where it determines the final particle radius. For the standard Fe/OA-ratio the particles grow to the largest radius.

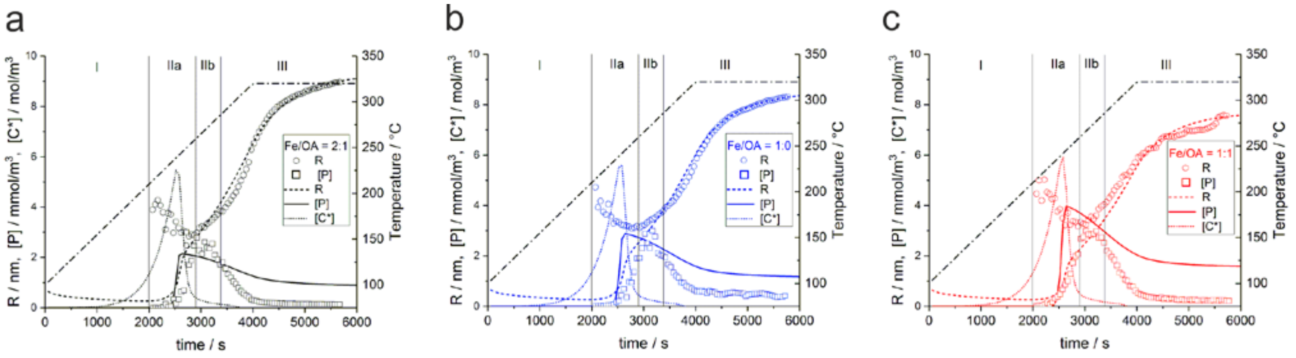

Fig. 5: Experimental growth curves R(t) (O) and relative particle concentrations $[P_{rel}](t)$ (☐) for oleate : oleic acid (Fe/OA) ratios of 2:1 (a, black), 1:0 (b, blue), and 1:1 (c, red) for a heating rate of 3.3 K/min and a plateau temperature of 320°C together with model calculations for the growth curves R(t) (dashed line), relative particle concentrations [P](t) (solid line), and transient phase concentrations [C*] = [FeO*] (dotted lines) for the non-classical NG-model. The dashed-dotted line indicates the temperature ramp (right y-axis). We observe that the non-classical NG-model nearly quantitatively describes the growth curves R(t) and provides a good description of the temporal evolution of the amorphous transient states [C*] and the aggregation processes for all Fe/OA-ratios. For all model calculations the transient phase is presently only present in Phase IIa. Aggregation processes start in Phase IIb and end in early Phase III.

From the calculated curves we observe that the differences in the growth Phase III actually are rooted in the different number of nuclei formed during Phase II. The fact that both higher and lower Fe/OA-ratios increase the particle number and therefore reduce the final radius indicates the existence of two effects of the Fe/OA-ratio on the particle number and radii. A large excess of oleic acid, corresponding to a lower Fe/OH-ratio, can form a steric barrier at the nanoparticle surface that limits precursor diffusion to the surface and therefore growth. This explains the low growth rates observed in Phase III for 1:1 A very low excess of oleic acid leads to less nuclei stabilization corresponding to high oversaturation, which leads to higher particle concentrations. At the optimum Fe/OA-ratio the nuclei are sufficiently stabilized, but the chosen excess of oleic acid does not yet limit precursor diffusion to the nanoparticle surface, which is necessary for sufficient growth such that Phase III is reached soon after the particle aggregation process has finished.

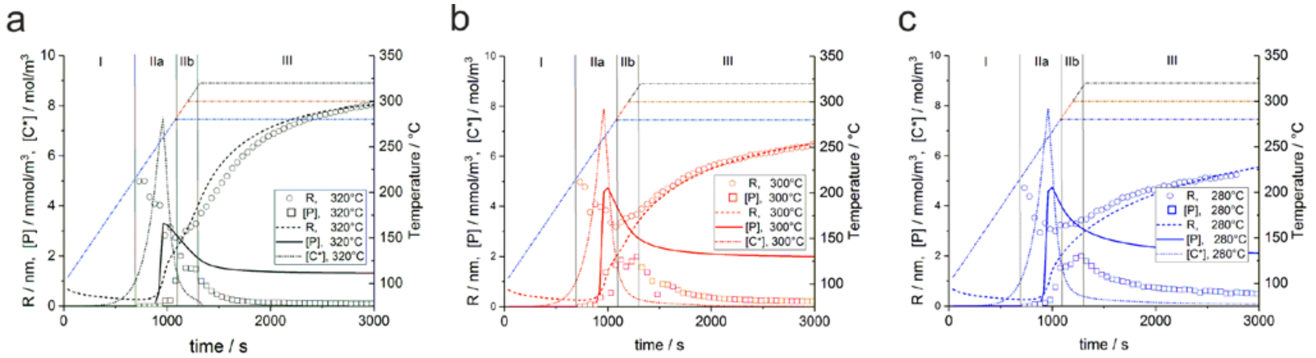

Fig. 6: Experimental growth curves R(t) (○) and relative particle concentrations [P_{rel}](t) (□) for plateau temperatures of 320°C (a, black), 300°C (b, red), and 280°C (c, blue) for a heating rate of 10 K/min and a Fe/OA-ratio of 2:1 together with model calculations for the growth curves R(t) (dashed line), relative particle concentrations [P](t) (solid line), and transient phase concentrations [C*] = [FeO*] (dotted lines) for the non-classical NG-model. The dashed-dotted line indicate the temperature ramp for the different plateau temperatures (right y-axis). We observe that the non-classical NG-model nearly quantitatively describes the growth curves R(t) and provides a good description of the temporal evolution of the amorphous transient states [C*] and the aggregation processes for all plateau temperatures.

Variation of the plateau temperature

Finally, also the plateau temperature provides important insights into the growth kinetics. We varied the plateau temperature T_b from 320°C, which is the boiling temperature of the solvent 1-octadecene, to 300°C and 280°C. From Fig. 6 we observe, that a reduction of the plateau temperature primarily affects the growth and aggregation rates, such that the highest plateau temperature furthers growth, thus leading to the formation of the largest particles.

As outlined above, the parameters in Table I were all kept constant for fitting the classical or non-classical NG-models to the experimental growth curves. For the final fit the only adjustable parameter was the T Arrhenius growth rate constant prefactor $k_{gr,0}$. The fitted values for each of the growth curves are summarized in Table II, together with the corresponding reaction conditions.

To compare the derived growth rate constants to values reported in literature we selected the value of k_{gr} at temperature of 280°C corresponding to the middle region of the growth phase. For our oleate-based iron oxide nanoparticle synthesis we observe growth rate constants in the range of $k_{gr} = 2.4 – 3.9\cdot10^{-6}$ m/s, which is faster compared to the iron pentacarbonyl-based iron oxide synthesis [25] with values of $k_{gr} = 1.5 – 2.6\cdot10^{-7}$ m/s. Similar or higher growth rate constants have been determined for Au with $k_{gr} = 1\cdot10^{-6}$ m/s

[13] and $k_{gr} = 2 \cdot 10^{-4}$ m/s as well as for ZnO with values of $k_{gr} = 0.6 – 4 \cdot 10^{-5}$ m/s. It shows that growth rate constants can vary over a range of $k_{gr} = 10^{-7}–10^{-4}$ m/s depending on the particle surface growth chemistry.

Table II: Reaction conditions and fitted growth rate constants for all experiments. $\dot{T}$ is the heating rate, T_b the plateau temperature, Fe/OA the iron/oleate molar ratio, t_b the time when the plateau temperature is reached, $k_{gr,0}$ is the Arrhenius growth rate constant prefactor (Eq. 16b) determined by non-classical NG theory (ncNG), and k_{gr} is the corresponding growth rate at 280°C for comparison to literature values and other experiments. cNG indicates the $k_{gr,0}$-values obtained by classical NG theory (cNG).

$\dot{T}$ K/min	T_b °C	Fe/OA	t_b s	$k_{gr,0}$ / m/s ncNG	k_{gr} / m/s @ 280°C	$k_{gr,0}$ / m/s cNG
3.3	320	2 : 1	4000	$8.3 \cdot 10^{4}$	$3.4 \cdot 10^{-6}$	$1.27 \cdot 10^{5}$
10	320	2 : 1	1320	$9.5 \cdot 10^{4}$	$3.9 \cdot 10^{-6}$	$1.65 \cdot 10^{5}$
20	320	2 : 1	660	$9.6 \cdot 10^{4}$	$3.9 \cdot 10^{-6}$	$1.70 \cdot 10^{5}$
10	300	2 : 1	1200	$7.5 \cdot 10^{4}$	$3.1 \cdot 10^{-6}$	
10	280	2 : 1	1080	$7.5 \cdot 10^{4}$	$3.1 \cdot 10^{-6}$	
3.3	320	1 : 0	4000	$5.8 \cdot 10^{4}$	$2.4 \cdot 10^{-6}$	
3.3	320	1 : 1	4000	$7.0 \cdot 10^{4}$	$2.9 \cdot 10^{-6}$	

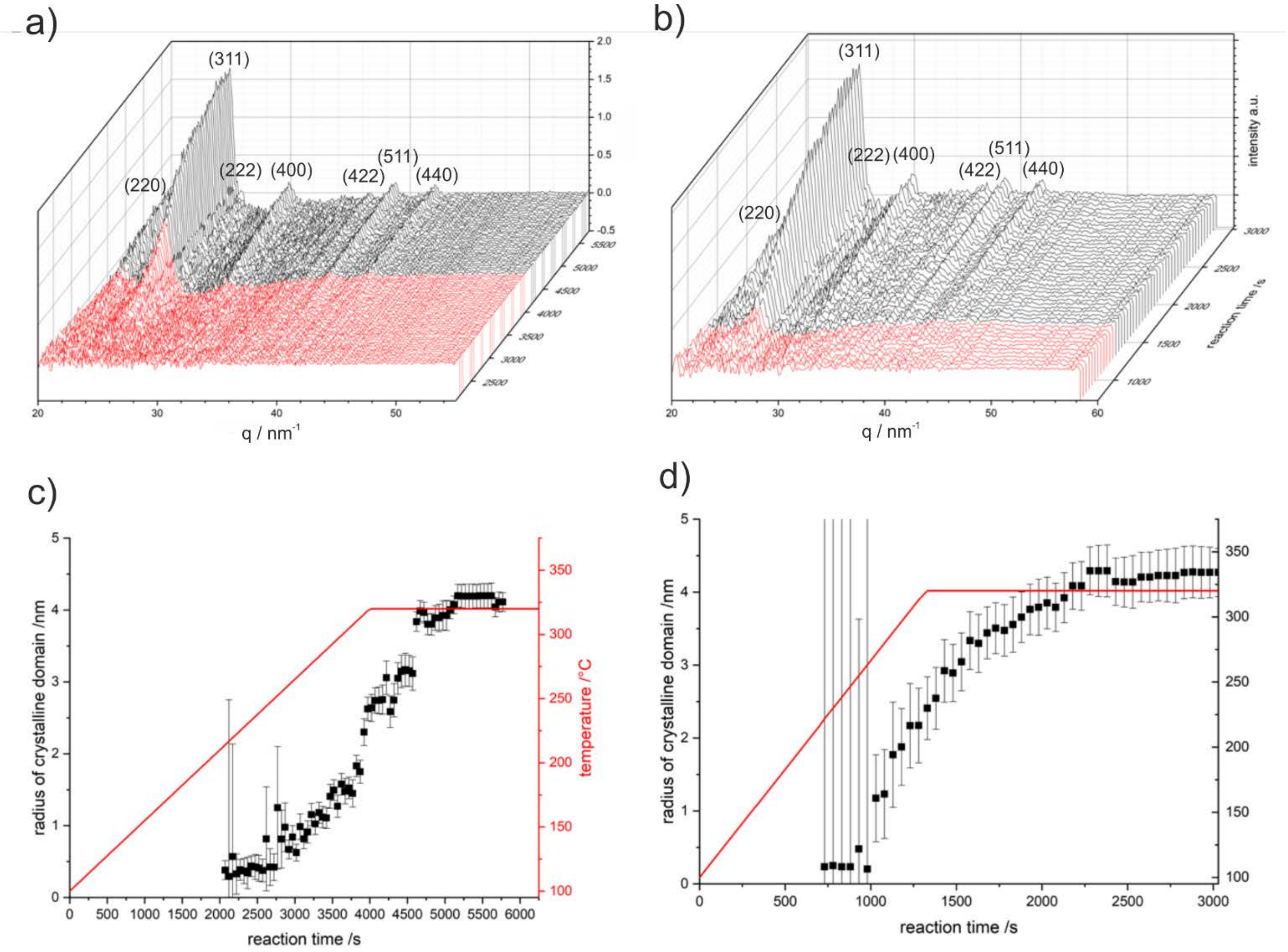

Fig. 7: WAXS-curves (a, b) and evolution of the crystalline domain size (c, d) for heating rates of 3.3 K/min (a, c) and 10 K/min (b, d). The peaks (220), (311),(222), (400), (422), (551), (440) can be indexed based on the space group Fd3m (spinel) of magnetite. The red colored diffraction curves were measured during the heat-up phase, the black colored diffraction curves during the temperature plateau phase.

In situ Wide-Angle X-ray Scattering (WAXS)

Using the high-temperature setup described in Fig. 9, we also followed the emergence of the wide-angle X-ray scattering (WAXS) signals *in situ* during the heat-up synthesis while simultaneously monitoring the SAXS intensity. Figs. 8a,b show the measured diffraction curves as a function of reaction time at a heating rate of 3.3 and 10 K/min, and a plateau temperature of 320°C. During the heat-up synthesis we observe the development of distinct Bragg peaks indicating the formation of crystalline nanoparticles. The peak positions correspond to the crystalline lattice of magnetite (Fe_3O_4) [25]. The observed reflections can be indexed as (220) (q = 21.3 nm^{-1}), (311) (q = 25.0 nm^{-1}), (400) (q = 30.2 nm^{-1}), (422) (q = 37.0 nm^{-1}),

(511) (q = 39.2 nm^{-1}) and (440) (q = 42.7 nm^{-1}) corresponding to cubic spinel crystal structure (Fd3m) with a unit cell of 0.833 nm, very similar to maghemite, which has the same crystal structure.

During heating up, indicated in red in Figs. 8 a,b, we observe the emergence of an initially quite broad peak at q = 25.0 nm^{-1}, which later develops into the (311) reflection. The broad peak becomes first noticeable at t* = 2100 s at a heating rate of 3.3 K/min (Fig. 7a), and at t*=700s at a heating rate of 10 K/min (Fig. 7b). The peak sharpens, rises in intensity and higher order peaks become noticeable for t** = 2800 s for 3.3 K/min, and for 1100 s for a heating rate of 10 K/min, indicating the development of crystalline nanoparticles. The temporal evolution of the diffraction curve for other reaction conditions is provided in the Supporting Information (Fig. S7), showing a very similar behavior. The characteristic times t* and t** are summarized for different heating rates in Table III. A comparison to the characteristic times t^I, t^{II}, and t^{III} derived from the time evolution of the radii and the relative particle concentrations reveals that the initial broad peak is observed in Phase IIa and t** corresponds to the start of Phase IIb.

We quantitatively analyzed the first three visible Bragg reflections (220, 311, 222) using the crystal structure of magnetite to calculate the radial structure factor in the powder average including the Debye-Waller factor, diffusive scattering as well as broadening due to the crystalline domain size. The details of this procedure are described in the Supporting Information. The derived domain sizes are shown in Fig. 8c, where the crystalline domain size is plotted as function of time. The growth curves of the crystalline domains D(t) can be well compared to the R(t) growth curves in Fig. 4. We note in particular the noticeable kink in the growth curve for a heating rate of 3.3 K /min at t=3600 s, indicating the start of Phase III.

We observe that the derived average crystalline domain sizes are systematically smaller compared to nanoparticle radii R. We therefore used TEM at high resolution to image the crystalline domains. As can be observed in Fig. 8, the nanoparticles are in general single crystals, with no obvious defect structures that would separate smaller crystalline domains. We can, however, not rule out the presence of amorphous core or peripheral domains, although – as in Fig. 8b – also the outer domain appears to have a well-developed crystalline structure.

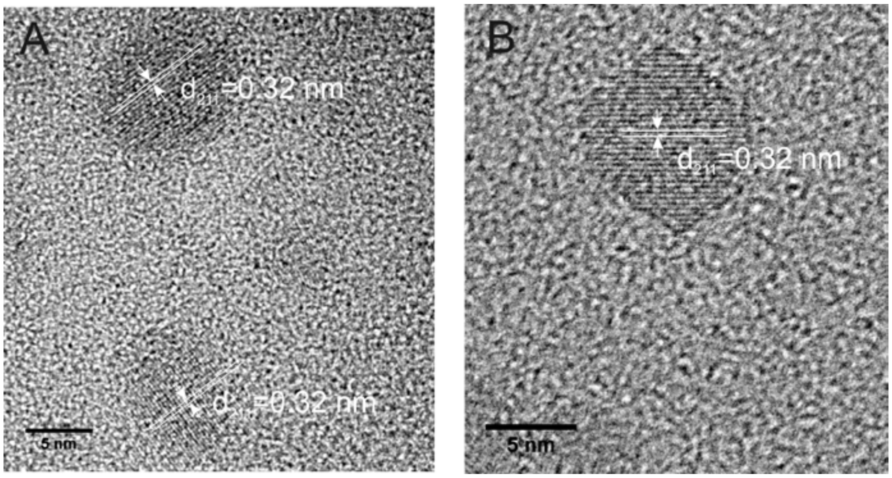

Fig. 8: TEM-images at high resolution showing the d_{211} = 0.32 nm lattice periodicity of the Fe_3O_4 magnetite crystal structure.

Characteristic nucleation and growth phases

From our *in situ* SAXS/WAXS heat-up experiments we have determined characteristic times t^{I}, t^{II}, t^{III}, t^{*}, and t^{**} related to distinct features in evolution of the particle radii, relative particle concentration, and crystalline domain sizes. These include the first appearance of Bragg peaks in the diffraction curves (t^{*}), the first appearance of excess small-angle scattering (t^{I}), the first narrowing of the (311)-reflection (t^{**}), as well as the minimum (t^{II}) and the kink (t^{III}) in the R(t) growth curve. The characteristic time are summarized in Table III.

Table III: Characteristic times and temperatures for the Phases I, II, III for different heating rates; t*: appearance of amorphous nuclei (WAXS), t^{I}: start of phase I (SAXS), t**: appearance crystalline nuclei (WAXS), t^{II}: start of phase II, t^{III}: start of phase III

	SAXS R(t)	**SAXS** [P_{rel}](t)	**WAXS** D(t)	Time at $\dot{T} = 3.3$ K/min	Time at $\dot{T} = 10.0$ K/min	Time at $\dot{T} = 20.0$ K/min
Phase I Induction Phase						
Phase IIa Formation of amorphous particles						
t*			First broad peak	2100 s	700 s	
t^{I}	First significant SAXS-curve			2000 s	700 s	400 s
T^{I}				210 °C	215 °C	230 °C
Phase IIb Formation of crystalline particles						
t**			(311)-reflection narrows	2800 s	1100 s	
t^{II}	R(t) minimum	[P_{rel}](t) maximum		2800 s	1100 s	600 s
T^{II} / °C				254 °C	283 °C	300 °C
Phase III Growth phase						
t^{III} / s	Kink in growth curve			3500 s	1350 s	
T^{III} / °C				290 °C	320 °C	

We observe that t* and t^{I}, as well as t** and t^{II} coincide very well for all reaction conditions, which is used to define the characteristic growth phases I, IIa, IIb, and III. The first Phase I is the induction phase where the precursor oversaturates, but not yet sufficiently to induce nucleation. Phase II is the nucleation and growth phase, where in Phase IIa an amorphous phase forms, that subsequently dissociates when in Phase IIb crystalline nanoparticles are formed. Consistently, Phase IIa with the presence of an amorphous phase is characterized by a weak and broad Bragg peak in the diffraction curve with weak small-angle excess scattering I(0). The dissociation of the amorphous phase or the amorphous clusters is observed towards the end of Phase IIa, indicated by the decrease of the measured radii R(t) until it reaches a minimum. In Phase IIb we observe the burst nucleation of crystalline nanoparticles indicated by (i) the narrowing and the increase of the (220)-reflection, (ii) the development of higher order peaks, and (iii) the initially strongly increasing small-angle scattering intensity.

In Phase III, the final growth phase, the crystalline nanoparticles grow in size until the precursor has been consumed. In Phases IIb and III the decrease in the particle concentration $[P_{rel}](t)$ indicates aggregation. The reduction in the particle concentration is consistent with the concomitantly observed increase in particle size. In case of aggregation, an n-fold reduction in the particle number should result in a $n^{1/3}$-fold increase in the particle radius. Therefore, a 4-fold reduction from 0.0004 (1100s) to 0.0001 (1500s) mol/m^3 should results in a $4^{1/3}$~1.59-fold increase of the particle radius, *i.e.* from 2.1 nm to 3.33 nm, which is in good agreement as observed in Fig. 5. Since the particle aggregation could be successfully described as a closed association process with a small final aggregation number, together with the corresponding activation energy, it likely corresponds to oriented particle attachment. This is further supported by the TEM images showing a faceted appearance of the nanoparticles. The corresponding extension of classical NG theory with the consideration of reversible amorphous particle formation and particle aggregation thus provides a very good and consistent description of the nucleation and growth process during heat-up synthesis.

The characteristic phases I, IIa, IIb, and III have been determined from characteristic times t^{I}, t^{II}, t^{III}, t^{*}, and t^{**} derived empirically from a large set of experimental data for systematically varying reaction conditions. It is satisfying to see that the phases can also be recognized in the growth curves calculated from the non-classical NG model. There is an induction Phase I with negligibly small particle radii and particle concentrations, where the oversaturation increases. Phase IIa is characterized by the appearance and subsequent disappearance of the transient amorphous state [C*]. The disappearance starts concomitantly with the burst nucleation of the crystalline nanoparticles. Phase IIb is characterized by initial particle growth due to precursor consumption as well as aggregation, leading to a decreasing number of particles. Phase III then is dominated by particle growth *via* monomer consumption until the monomer has been completely consumed. Thus, the observed characteristic growth phases are well supported by a non-classical NG model that includes amorphous precursor formation and particle aggregation.

Growth model and comparison to literature

It is instructive to compare the observed nucleation and growth phases with similar phases described in literature. Classical NG models have been successfully developed and used to describe nanoparticle nucleation and growth processes. [22] This has been clearly demonstrated for the synthesis of CdSe nanoparticles. As considered in the classical NG model, Cd- and Se-precursor sources react to generate a (CdSe)-species which supersaturates and (i) either nucleates particles in the form of $(CdsSe)_n$-units, or (ii) adds to existing growing particles $(CdsSe)_{n'}$. [23,39] The same classical mechanism has been reported for Au-nanoparticles, where a Au^{3+}-precursor source (e.g. $HAuCl_4$) reacts to form a (Au^0)-species, which supersaturates and (i) either nucleates new Au-nanoparticles or (ii) integrates into growing Au-nanoparticles. [4,6,13,24]. The classical mechanism has also been found to apply for the formation of Pd-nanoparticles. [16] Non-classical nucleation and growth phenomena that have been observed and considered in kinetic models are ligand binding [40,41], aggregative growth [8,11,12,40,42], amorphous precursor formation [17-19,21,25,43], oriented attachment [2,38,44], and secondary nucleation [17-19,21].

The classical NG-model considers simple species such as (CdSe), (Au^0) or $Fe(OA)_m$ as reactive precursors that supersaturate and (i) integrate into new nuclei or (ii) growing particles. This is indicated by the route A) in Fig. 1. For many oxidic nanoparticles the formation of larger amorphous polymetal-oxo-clusters Me_xO_y has been reported. These clusters can be considered as larger (Me_xO_y)-species that supersaturate and subsequently nucleate or add to growing crystalline particles, following the classical route. In Fig. 1 this is indicated by the route B). The formation of these clusters has been reported by Lassenberger *et al.* [25] and Baumgärtner *et al.* [45] for the synthesis of iron oxide nanoparticles [25], and by Caetano *et al.* in the form of Zn-oxy-acetate for the synthesis of ZnO- [17-19], and similarly for polynuclear tin-oxo-halide SnO-precursor nanoparticles. [21]

If the formed amorphous clusters are larger, they may constitute distinct particles or amorphous domains. This is considered by the reversible formation of the transient domains indicated by C) in Fig. 1. At high supersaturation the formation of these particles or domains can proceed fast, reversible, and with low activation energy. It can thus be represented by a fast chemical equilibrium [22]. These are termed pre-nucleation clusters [46], particles or phases, or liquid precursor phases. [2,47] Subsequent nucleation of crystalline particles can proceed by re-dissociation of the amorphous precursor particles as has been observed for $CaCO_3$ [43], corresponding to the back reaction in Fig. 1. Alternatively, the amorphous domains can themselves be the location for the nucleation of the crystalline particles. This is indicated by the dashed line in Fig. 1. In the non-classical nucleation and growth model the nucleation term (Eq. 15d) would then depend on the supersaturation S and the interfacial tension γ of the crystalline particles in the liquid precursor or amorphous phase. Prior to the nucleation of a crystalline phase, densification and dehydration steps are frequently observed for metal oxides. The formation of a liquid precursor phase with subsequent nucleation has been clearly demonstrated experimentally [2,48-51]. If the formation of the amorphous particles proceeds with a higher energy barrier, this could involve a distinct nucleation step. The subsequent nucleation of the crystalline particles is then considered as secondary nucleation. [21] In reality, it is likely that there are continuous variations from simple 'monomeric' precursor species A) evolving into polynuclear and amorphous domains B). If sufficiently large, they become distinct particles or domains, which may eventually be the location for nucleation, which in the classical model is homogeneously occurring only in solution. Thus routes A), B), and C) in the non-classical NG model in Fig. 1 systematically describe the most common nucleation pathways found for nanoparticles.

Aggregative growth is regularly observed in solution and under atmospheric conditions. Cluster-cluster aggregation has clearly been reported for ZnO- and SnO-nanoparticles [17,21]. In addition, oriented attachment is a very common and important aggregation processes involved in the formation of nanoparticles [2,36-38,44]. As shown in Fig. 1, it is straightforward to integrate aggregation processes into a NG-model. Approximations such as cohort averaging can be made to keep it computationally tractable.

Depending on the relative rates of each elemental nucleation, growth and aggregation step, there can be smooth transitions between different nucleation and growth scenarios, with a system of pathways outlined in Fig. 1. It is thus not surprising, that different phase sequences that have been identified experimentally are largely consistent with these pathways.

Conclusions

With a developed heating setup it is possible to perform *in situ* simultaneous SAXS/WAXS experiments to investigate the nucleation and growth of iron oxide nanoparticles during the commonly used heat-up synthesis up to temperatures of 320°C covering the complete reaction time from the early nucleation to the late growth phase. The experiments allowed to determine the growth curve R(t), the relative particle concentration $[P_{rel}](t)$ and the changes in nanoparticle crystallinity for systematically varied heating rates, ligand concentration and plateau temperatures.

We show that the classical NG model can be extended to a non-classical NG model that takes into account (i) the reversible formation of a transient state, and (ii) the aggregation of nanoparticles to form stable aggregates, such as during oriented attachment. Furthermore, we considered (iii) the temperature-dependence of the kinetic parameters *via* an Arrhenius-ansatz to quantitatively model heat-up and hot-injection nanoparticle synthesis. This extended non-classical nucleation and growth model successfully describes all measured growth curves R(t) and the observed variations in $[P_{rel}](t)$ as well as the temporal evolution of the crystallinity. Introducing the concept of cohort averaging allowed an efficient computation of simultaneous nucleation, growth and aggregation.

The measured growth curves R(t), the variations of the relative particle concentrations [P](t) and the temporal evolution of the crystalline domain sizes D(t) allowed to clearly distinguish three distinct kinetic phases, *i.e.* the induction Phase I, the final growth Phase III, and an intermediate Phase II, which can be further divided into an early Phase IIa with the presence of an amorphous transient state, and a late Phase IIb, where crystalline particle nucleation and aggregation occurs. These empirically assigned phases can be congruently related to phases in the non-classical kinetic model, corresponding evolution of the transient state in Phase IIa and aggregation processes in Phase IIb and early Phase III.

Practical conclusions that can be drawn for designing a heat-up synthesis are that the heating rate should be designed that Phase IIa and thus nucleation and growth sets in halfway through the heating ramp such that the final growth Phase III starts when reaching the final ramp temperature. This ensures that amorphous precursor and aggregation states have been passed through, when the monomer growth dominating final phase has started.

The described extension of the classical NG model takes into account the two most important features of non-classical NG routes, *i.e.* the formation of intermediate or transient species, and particle aggregation processes. The described *in situ* experiments together with the non-classical NG model thus open the way to quantitatively understand, predict and control nanoparticle nucleation and growth kinetics for a wide range of nanoparticle systems and synthetic procedures.

Methods/Experimental

Nanoparticle synthesis

The general synthesis route is based on the procedure developed by Hyeon *et al* [26]. For the preparation of the iron oleate, iron(III) chloride hexahydrate (Aldrich, puriss p.a. ACS reagent, ≥99.8%) and sodium oleate (TCI, >97%) were dissolved in a mixture of ethanol (VWR, 96%), deionized water and heptane (Aldrich, reagent grade, 99%) and subsequently heated to 70 °C. The mixture was kept at 70 °C for 4 h and then washed with deionized water three times and dried under vacuum.

For the preparation of the precursor solutions used in the *in situ* experiments iron(III) oleate and oleic acid (Aldrich, technical grade, 90 %, amounts given in Table 3-1) were dissolved in 50 mL of 1-octadecene (Aldrich, for synthesis) and heated to 100 °C under vacuum. Three different iron(III) oleate : oleic acid molar ratios of 8 : 4 mmol (‘standard’), 8 : 8 mmol, and 8 : 0 mmol were investigated. For simplicity, in text we refer to relative compositions of 2:1 (8 : 4 mmol), 1:1 (8 : 8 mmol), and 1:0 (8 : 0 mmol). For purging, the solution was kept at 100 °C under vacuum for 1 h. After cooling to room temperature, the precursor solution was ready for use.

Heat-up synthesis sample preparation

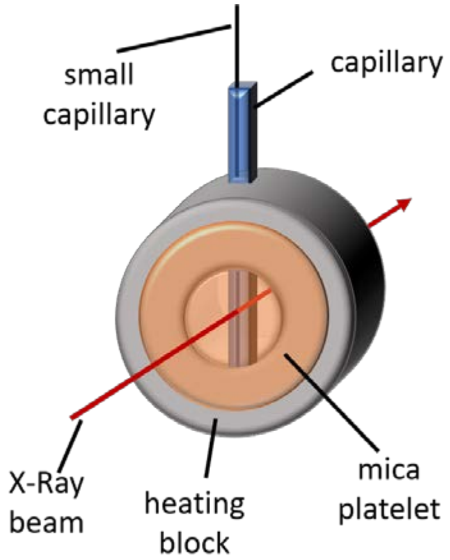

Fig. 9: Capillary setup consisting of thin glass capillary, in which the heat-up synthesis is carried out. In the heating block the reaction solution is heated to 320°C, the boiling temperature of the solvent. Mica sheets reduce temperature losses due to convection. A small capillary is inserted to nucleate and guide small gas bubbles to prevent beam interference. The direction of the X-ray beam perpendicular to the capillary is indicated.

For the individual measurements, the precursor solution was filled into a boron-glass capillary with a diameter of 1.5 mm and a wall thickness of 0.01 mm (Fig. 9). The filling height was chosen in such a way that the level of the solution was equal or below the upper edge of the heating block. The system used for heating was a modified Linkam HT-600 setup. A hole of ~2mm diameter was drilled through the heating block to be able to insert glass capillaries of 1.5mm diameter. The bottom hole of the heating block was closed with a plug made from aluminum foil so that the capillary stayed in place. A capillary with a diameter of 0.5 mm was inserted into the filled 1.5 mm capillary to prevent overheated boiling and the formation of gas bubbles blocking the X-ray beam. Before each experiment the beam position was adjusted slighlty as to not hit the small capillary. The heating block was then heated from 100 °C to the end temperature with a defined heating rate and kept at the end temperature for a defined time span. To reach temperatures of up to 320°c, the boiling temperature of the solvent, we found it necessary to attach mica sheets to minimize temperature losses due to convection (Fig. 9). Heating rates of 10 K/min, 3.3 K/min (‘standard’) and 20 K/min were investigated, with end temperatures of 320°C (‘standard’), 300°C, and 280°C. The Linkam HT-600 was directly controlled with the same software as the SAXS data aquisition (CERTIF SPEC) so that heating/temperature correlations to the acquired data was seamless.

After the experiment the capillaries were cooled to room temperature, the reacted solution was mixed with THF and precipitated with ethanol. The nanoparticles were then redispersed in THF and the TEM samples were prepared by dropping 4 μL of solution on a carbon-coated copper grid. TEM was performed with a JEOL F200 at 200 kV.

Small-angle and wide-angle X-ray scattering (SAXS, WAXS)

The SAXS measurements were carried out on the in-house SAXS system 'Ganesha Air' from SAXSLAB/XENOCS. The X-ray source was a D2-MetalJet operating at 70 kV and 3.57 mA, emitting Ga-Kα radiation with a wavelength of 0.13414 nm. The SAXS detector was a Pilatus 300 k (Dectris) and the WAXS detector a Pilatus 100 k (Dectris). The frame time, the time for one measurement, was set to 10 s with a dead time of ~0.1s between the frames. For analysis five consecutive frames were averaged to give a better signal to noise ratio while still keeping a reasonable resolution with respect to reaction time. As the solution is undergoing constant change throughout the reaction, choosing the right background is not straightforward. The solution at a 100°C has not reacted and would seem a good candidate for a background, but at higher *q*-values the signal is always higher than at the end of the reaction. As a compromise we chose the curves at 215°C to use as background. At this temperature the iron oleate complex is still intact and no nanoparticles or clusters have been formed. In all 2D scattering patterns the beam stop and beam stop arm were masked as well as the blank spaces between the detector banks. Then the 2D images were radially averaged and normalized for measurement time. After background subtraction with error propagation the data were fitted. All primary data processing and fitting was done using Jscatter [27].

Wide-angle X-ray scattering was carried out simultaniously on the same scattering volume by positioning the WAXS detector at an approximate angle of ~60° with respect to the beam direction at a distance of ~5cm from the sample. The WAXS setup was calibrated using silicon as a standard material. The data treatment and background subtraction was handled in the same way as for the SAXS data including corrections for the larger scattering angles. A detailed description of all data treatment and the fitting procedures is given the Supporting Information.

Thermogravimetric Analysis (TGA)

The TGA measurements were carried out with a TG 209 *F1 Libra* from Netzsch. The samples were heated from 25 °C to 400 °C with a defined heating rate under nitrogen atmosphere. The software *Proteus* was used for the data evaluation.

Associated Content

Supporting Information

The Supporting Information is available free of charge at https://pubs.acs.org/doi/acsnano....

It provides details on the nucleation and growth algorithm, validation of the algorithm against published experimental data, as well as further information on data treatment and analysis.

Author Information

Corresponding Author

Stephan Förster – JCNS-1/IBI-8, Forschungszentrum Jülich, 52428 Jülich, Germany; Institute of Physical Chemistry, RWTH Aachen University, 52074 Aachen, Germany;

ORCID: 0000-0002-7323-2449; Phone: +49-2461-6185161; email: s.foerster@fz-juelich.de

Acknowledgements

Financial support from the German Science Foundation (DFG) *via* the SFB 840 is gratefully acknowledged.

Conflicts of interest

The authors declare no conflicts of interests.

References

[1] Boles, M. A.; Engel, M.; Talapin, D. V. Self-assembly of colloidal nanocrystals: from intricate structures to functional materials, Chem. Rev. 2016, 116, 11200-11289.

[2] De Yoreo, J. J.; Gilbert, P. U. P. A., Sommerdijk, N. A. J. M.; Penn, R. L.; Whitelam, S.; Joester, D.; Zhang, H.; Rimer, J. D.; Navrotsky, A.; Banfield, J. F.; Wallace, A. F.; Michel, F. M.; Meldrum, F. C.; Cölfen, H.; Dove, P. M. Crystallization by particle attachment in synthetic, biogenic, and geologic environments, *Science* 2015, 349, 6247

[3] Hubert, F.; Testard, F.; Thill, A.; Kong, Q.; Tache, O.; Spalla, O. Growth and overgrowth of concentrated gold nanorods: time resolved SAXS and XANES. Cryst. Growth Des. 2012, 12, 1548−1555.

[4] Abécassis, B.; Testard, F.; Kong, Q.; Francois, B.; Spalla, O. Influence of monomer feeding on a fast gold nanoparticles synthesis: time-resolved XANES and SAXS experiments. Langmuir 2010, 26, 13847−13854.

[5] Abécassis, B.; Testard, F.; Spalla, O. Gold nanoparticle superlattice crystallization probed *in situ*. Phys. Rev. Lett. 2008, 100, 115504.

[6] Abécassis, B.; Testard, F.; Spalla, O.; Barboux, P. Probing *in situ* the nucleation and growth of gold nanoparticles by small-angle X-ray scattering. Nano Lett. 2007, 7, 1723−1727.

[7] Polte, J.; Erler, R.; Thünemann, A. F.; Sokolov, S.; Ahner, T. T.; Rademann, K.; Emmerling, F.; Kraehnert, R. Nucleation and growth of gold nanoparticles studied *via in situ* small angle X-ray scattering at millisecond time resolution. ACS Nano 2010, 4, 1076−1082.

[8] Polte, J.; Erler, R.; Thünemann, A. F.; Emmerling, F.; Kraehnert, R. SAXS in combination with a free liquid jet for improved timeresolved *in situ* studies of the nucleation and growth of nanoparticles. Chem. Commun. 2010, 46, 9209−9211.

[9] Polte, J.; Kraehnert, R.; Radtke, M.; Reinholz, U.; Riesemeier, H.; Thünemann, A. F.; Emmerling, F. New insights of the nucleation and growth process of gold nanoparticles *via in situ* coupling of SAXS and XANES. J. Phys.: Conf. Ser. 2010, 247, 012051.

[10] Polte, J.; Emmerling, F.; Radtke, M.; Reinholz, U.; Riesemeier,H.; Thünemann, A. F. Real-time monitoring of copolymer stabilized growing gold nanoparticles. Langmuir 2010, 26, 5889−5894.

[11] Polte, J.; Ahner, T. T.; Delissen, F.; Sokolov, S.; Emmerling, F.; Thünemann, A. F.; Kraehnert, R. Mechanism of gold nanoparticle formation in the classical citrate synthesis method derived from coupled *in situ* XANES and SAXS evaluation. J. Am. Chem. Soc. 2010, 132, 1296−1301.

[12] Koerner, H.; MacCuspie, R. I.; Park, K.; Vaia, R. A. *In situ* UV/Vis, SAXS, and TEM study of single-phase gold nanoparticle growth. Chem. Mater. 2012, 24, 981−995.

[13] Chen, X.; Schröder, J.; Hauschild, S.; Rosenfeldt, S.; Dulle, M.; Förster, S. Simultaneous SAXS/WAXS/UV-Vis study of the nucleation and growth of nanoparticles: a test of classical nucleation theory. Langmuir 2015, 31, 11678−11691.

[14] Chen, X.; Wei, M.; Jiang, S.; Förster, S. Two growth mechanisms of thiol-capped gold nanoparticles controlled by ligand chemistry, Langmuir 2019, 35, 12130-12138.

[15] Mozaffari, S.; Li, W.; Thompson, C.; Ivanov, S.; Seifert, S.; Lee, B.; Kovarik, L.; Karim, A. M. Colloidal nanoparticle size control: experimental and kinetic modeling investigation of the ligand-metal binding role in controlling the nucleation and growth kinetics.
Nanoscale 2017, 9, 13772.

[16] Wu, L.; Lian, H.; Willis, J. J.; Goodman, E. D.; McKay, I. S.; Qin, J.; Tassone, C. J.; Cargnello, M. Tuning precursor reactivity toward nanometer-size control in palladium nanoparticles studied by *in situ* small angle X-ray scattering, Chem. Mater. 2018, 30, 1127-1135.

[17] Caetano, B. L.; Santilli, C. V.; Meneau, F.; Briois, V.; Pulcinelli, S. H. *In situ* and simultaneous UV-Vis/SAXS/ and UV-vis/XAFS time-resolved monitoring of ZnO quantum dots formation and growth. J. Phys. Chem. C 2011, 115, 4404−4412.

[18] Caetano, B. L.; Santilli, C. V.; Pulcinelli, S. H.; Briois, V. SAXS and UV-Vis combined to quick-XAFS monitoring of ZnO nanoparticles formation and growth. *Phase Transitions* 2011, 84, 714−725.

[19] Caetano, B. L.; Briois, V.; Pulcinelli, S. H.; Meneau, F.; Santilli, C. V. Revisiting the ZnO Q-dot formation toward an integrated growth model: from coupled time resolved UV-Vis/SAXS/XAS data to multivariate analysis. *J. Phys. Chem. C* 2017, 121, 886−895.

[20] Herbst, M.; Hofmann, E.; Förster, S. Nucleation and growth kinetics of ZnO nanoparticles studied by *in situ* microfludic SAXS/WAXS/UV-Vis experiments, *Langmuir* 2019, 35, 11702-11709

[21] Caetano, B.; Meneau, F.; Santilli, C. V.; Pulcinelli, S. H.; Magnani, M.; Briois, V. Mechanism of SnO2 nanoparticle formation and growth in acid ethanol solution derived from SAXS and combined Raman-XAS time-resolved studies. *Chem. Mater.* 2014, 26, 6777-6785.

[22] Kwon, S. G.; Hyeon, T. Formation mechanisms of uniform nanocrystals *via* hot-injection and heat-up methods, *Small* 2011, 19, 2685-2702.

[23] Abécassis, B.; Bouet, C.; Garnero, C.; Constantin, D.; Lequeux, N.; Ithurria, S.; Dubertret, B.; Pauw, B. R.; Pontoni, D. Real-time *in situ* probing of high-temperature quantum dots solution synthesis. Nano Lett. 2015, 15, 2620−2626.

[24] Maes, J.; Castro, N.; de Nolf, K.; Walravens, W.; Abecassis, B.; Hens, Z. Size and concentration determination of colloidal nanocrystals by small-angle X-ray scattering, Chem. Mater. 2018, 30, 3952-3962.

[25] Lassenberger, A.; Grünewald, T. A.; van Oostrum, P. D. J.; Rennhofer, H.; Amenitsch, H.; Zirbs, R.; Lichtenegger, H. C.; Reimhult, E. Monodisperse iron oxide nanoparticles by thermal decomposition: elucidating particle formation by second-resolved *in situ* small-angle X-ray scattering, Chem. Mater. 2017, 29, 4511-4522.

[26] Park, J.; An, K.; Hwang, Y.; Park, J. E. G.; Noh, H. J.; Kim, J. Y., Park, J. H.; Hwang, N. M.; Hyeon, T., Ultra-large-scale synthesis of monodisperse nanocrystals, Nat. Mater. 2004, 3, 891 – 895.

[27] R. Biehl, Jscatter, a program for evaluation and analysis of experimental data, PLoS One 2019, 14, e0218789.

[28] LaMer, V. K. Nucleation in Phase Transitions, *Ind. Eng. Chem*. 1952, 44, 1270-1277.

[29] Finney, E. E.; Finke, R. G. Nanocluster nucleation and growth kinetic and mechanistic studies: a review emphasizing transition-metal nanoclusters, J. Coll. Interface Sci. 2008, 317, 351-374.

[30] Chu, D. B. K.; Owen, J. S.; Peters, B. Nucleation and growth kinetics from LaMer burst data, J. Phys. Chem. A 2017, 121, 7511-7517.

[31] Talapin, D. V.; Rogach, A. L.; Haase, M.; Weller, H. Evolution of an ensemble of nanoparticles in a colloidal solution: Theoretical study. J. Phys. Chem. B 2001, 105, 12278-12285.

[32] van Embden, J.; Sader, J. E.; Davidson, M.; Mulvaney, P. Evolution of colloidal nanocrystals: theory and modeling of their nucleation and growth. J. Phys. Chem. C 2009, 113, 16342-16355.

[33] Mantzaris, N. V. Liquid-phase synthesis of nanoparticles: particle size distribution dynamics and control. Chem. Eng. Sci. 2005, 60, 4749-4770.

[34] Rempel, J. Y.; Bawendi, M. G.; Jensen, K. F. Insights into the kinetics of semiconductor nanocrystal nucleation and growth, J. Am. Chem. Soc. 2009, 131, 4479-4488.

[35] Smoluchowski, M. Drei Vorträge über Diffusion, Brownsche Molekularbewegung und Koagulation von Kolloidteilchen, *Phys. Z.* 1916, 17, 557-571.

[36] Zhang, J.; Lin, Z.; Lan, Y.; Ren, G.; Chen, D.; Huang, F.; Hong, M. A multistep oriented attachment kinetics: coarsening of ZnS nanoparticle in concentrated NaOH, *J. Am. Chem. Soc*. 2006, 128, 12981-12987.

[37] Zhang, J.; Wang, Y.; Zheng, J.; Huang, F.; Chen, D.; Lan, Y.; Ren, G.; Lin, Z.; Wang, C. Oriented attachment kinetics for ligand capped nanocrystals: coarsening of thiol-PbS nanoparticles, J. Phys. Chem. B 2007, 111, 1449-1454.

[38] Penn, R. L. Kinetics of oriented aggregation, J. Phys. Chem. B 2004, 108, 12707-12712.

[39] Owen, J. S.; Chan, E. M.; Liu, H.; Alivisatos, A. P. Precursor conversion kinetics and the nucleation of cadmium selenide nanocrystals, J. Am. Chem. Soc. 2010, 132, 18206-18213

[40] Wang, F.; Richards, V. N.; Shields, S. P.; Buhro, W. E. Kinetics and mechanisms of aggregative nanocrystal growth, Chem. Mater. 2014, 26, 5-21.

[41] Mozaffari, S.; Li, W.; Thompson, C.; Ivanov, S.; Seifert, S.; Lee, B.; Kovarik, L.; Karim, A. M. Colloidal nanoparticle size control: experimental and kinetic modeling investigation of the ligand-metal binding role in controlling the nucleation and growth kinetics. Nanoscale 2017, 9, 13772

[42] Harada, M.; Kizaki, S. Formation mechanism of gold nanoparticles synthesized by photoreduction in aqueous ethanol solutions of polymers using *in situ* quick scanning X-ray absorption fine structure and small-angle X-ray scattering, Cryst. Growth Des. 2016, 16, 1200-1212.

[43] Pontoni, D.; Bolze, J.; Dingenouts, N.; Narayanan, T.; Ballauff, M. Crystallization of calcium carbonate observed in-situ by combined small- and wide-angle x-ray scattering, J. Phys. Chem. B 2003, 107, 5123-5125.

[44] Schliehe, C.; Juarez, B. H.; Pelletier, M.; Jander, S.; Greshnykh, D.; Nagel, M.; Meyer, A.; Förster, S.; Kornowski, A.; Klinke, C.; Weller, H. Ultrathin PbS sheets by two-dimensional oriented attachment, Science 2010, 329, 550-553.

[45] Baumgartner, J.; Ramamoorthy, R. K.; Freitas, A. P.; Neouze, M.-A.; Bennet, M.; Faivre, D.; Carriere, D. Self-confined nucleation or iron oxide nanoparticles in a nanostructured amorphous precursor, Nano Lett. 2020, 20, 5001-5007.

[46] Ramamoorthy, R. K.; Yildirim, E.; Barba, E.; Roblin, P.; Vargas, J. A.; Lacroix, L.-M.; Rodriguez-Ruiz, I.; Decorse, P.; Petkov, V.; Teychene, S.; Viau, G. The role of pre-nucleation clusters in the crystallization of gold nanoparticles, Nanoscale 2020, 12, 16173.

[47] Vekilov, P. G. Nucleation, Crystal Growth Design 2010, 10, 5007-5019.

[48] Wohlrab, S.; Cölfen, H.; Antonietti, M., Crystalline, porous microspheres made from amino acids by using polymer-induced liquid precursor phases. Angew. Chem. Int. Ed. 2005, 44, 4087-4092.

[49] Smeets, P. J. M.; Finney, A. R.; Habraken, W. J. E. M.; Nudelman, F.; Friedrich, H.; Laven, J.; De Yoreo, J. J.; Rodger, P. M.; Sommerdijk, N. A. J. M. A classical view on nonclassical nucleation, Proc. Natl. Acad. Sci. 2017, 114, 7882-7890

[50] E. Wiedenbeck, M. Kovermann, D. Gebauer, H. Colfen. Liquid metastable precursors of Ibuprofen as aqueous nucleation intermediates. Angew. Chem. Int. Ed. 2019, 58 10103-19109.

[51] Kashchiev, D. Classical nucleation theory approach to two-step nucleation of crystals, J. Cryst. Growth 2020, 530, 125300.